Internal Redundancy of Mechanically Fastened Built-Up Steel Axially Loaded Two-Channel Members

Jason B. Lloyd, Francisco J. Bonachera Martin, Cem Korkmaz, and Robert J. Connor

ABSTRACT

Previous research on large-scale fracture tests on mechanically fastened built-up steel members subjected to flexural or axial loads demonstrated resistance to complete member fracture due to cross-boundary fracture resistance (CBFR). This paper builds on and expands that work through additional experimental and analytical research into behavior of two-channel mechanically-fastened built-up axial steel members following fracture of a single component. Finite element based parametric studies were conducted to characterize the static load redistribution behavior of axial members comprised of two channels, following a fracture event. FEMs were calibrated using experimental data obtained from full-scale testing. Simplified solutions were developed to estimate the after-fracture load capacity and the fatigue stress range in a remaining channel. The solutions are used to evaluate the internal redundancy of mechanically fastened built-up two-channel members. If this member type is found to be internally redundant during an evaluation, the developed solutions can then be used to reliably predict fatigue life of the member in the faulted state and establish the special inspection interval according to the relevant provisions of AASHTO.

Keywords: steel bridge, built-up steel members, nonredundant steel tension member, fracture critical member, internal redundancy, steel axial member.

INTRODUCTION

Since the Surface Transportation and Uniform Relocation Assistance Act of 1987 (Pub. L. 100-17, 101 Stat. 132), the AASHTO *Manual for Bridge Evaluation* (AASHTO, 2018) requires that bridges containing fracture critical members (FCMs) receive a "hands-on" inspection, meaning the inspector must be within an arm's length of any fracture critical component at least every 24 months (FHA, 1988). Fracture critical members have since been renamed nonredundant steel tension members (NSTMs) with an overhaul to the "National Bridge Inspection Standards" released in 2022 (FHA, 2022). NSTMs require the same level of inspection rigor as the FCMs, but the inspection interval may be shorter or longer, depending on a risk-based evaluation. The cost of hands-on inspections can be strenuous on state transportation budgets due to the time required on the bridges, traffic control during inspections, and specialized equipment required (Connor et al., 2005). Furthermore, while hands-on inspections of NSTMs are intended to improve public safety, a study carried out for Indiana interstates revealed that overall congested crash rates increased by 24.1 times over uncongested crash rates and that 90% of the congested crashes in 2014 occurred with a traffic queue duration of ≥ 5 minutes (Mekker et. al., 2015). Traffic queues of this magnitude can result from several things, including closed lanes on bridges during inspections. Protecting the safety of the traveling public is multifaceted—it isn't necessarily as simple as requiring more bridge inspection, particularly when one considers the probability of detection for very small defects intended to be found (Campbell et al., 2019). The approach to the nation's bridge inspection program should be rational—considering all the economic *and* safety factors and correlating damage tolerance with inspector capabilities.

Previous research that carried out large-scale fracture tests on mechanically fastened built-up steel members subjected to flexural or axial loads demonstrated resistance to complete member fracture due to cross-boundary fracture resistance (CBFR) (Hebdon et al., 2017; Lloyd et al., 2021). Additionally, Diggelmann et al. (2013) used shape charges to simulate fracture on the tension chord at midspan of the Milton-Madison deck truss approach span while the bridge was loaded with approximately 75 kips of sand placed on the middle third of the span. The chord was severed in two stages, the first of which cut one of the two built-up channels that made up the tension chord. Under the simulated live load, the researchers measured a global deflection of less than ⅛ in. After severing the remaining portion of the

Jason B. Lloyd, PhD, PE, Manager of Bridge & Infrastructure Solutions, Nucor, Charlotte, N.C. Email: jason.lloyd@nucor.com (corresponding author)

Francisco J. Bonachera Martin, PhD, PE, Technical Manager, Michael Baker International, Indianapolis, Ind. Email: FJ.BonacheraMartin@mbakerintl.com

Cem Korkmaz, PhD, Research Engineer, Lyles School of Civil Engineering, Purdue University, West Lafayette, Ind. Email: ckorkmaz@purdue.edu

Robert J. Connor, PhD, PE, Jack and Kay Hockema Professor, Lyles School of Civil Engineering, Purdue University, West Lafayette, Ind. Email: rconnor@purdue.edu

Paper No. 2023-01

tension chord, the bridge remained stable, and researchers measured a total deflection of less than ½ in. This is remarkable for a bridge that was in service for 91 years and a member identified as fracture critical and then required to be treated as such for the last 34 of those years.

This paper summarizes the experimental and analytical research into the behavior of two-channel mechanically fastened built-up axial steel members following fracture of a single channel. Finite element–based parametric studies were conducted to characterize the static load redistribution behavior of two-channel axial members following the fracture event. Finite element models (FEMs) were calibrated using experimental data obtained from full-scale testing. Simplified solutions were developed to estimate the after-fracture load capacity and the fatigue stress range in the remaining channel. The solutions can be applied to analyze for internal redundancy of these member types. If a member is found to be internally redundant, the simple solutions can then be used to reliably predict fatigue life of the member in the faulted state and establish the special inspection interval according to the provisions of AASHTO (2018).

Research Objectives

The primary objectives of the experimental testing were to understand the static load redistribution behavior in the faulted condition and calibrate finite element models for parametric study. The parametric studies were used to develop simplified engineering solutions for the evaluation of internal redundancy. In this case, the faulted condition is defined as having one-half of the total cross section severed. Brittle fracture testing was not necessary to achieve the test objectives. Furthermore, previous work on the internal redundancy of built-up members unequivocally demonstrated the inherent characteristic of mechanically fastened built-up members referred to as cross-boundary fracture resistance (CBFR) (Hebdon et al., 2017; Lloyd et al., 2021). CBFR provides brittle fracture arrest at component boundaries resisting total cross-sectional fracture. Therefore, in the present study, the fracture event was not necessary, and testing was performed by severing one-half of the unloaded chord using a cutting torch. Next, the specimens were statically loaded in the faulted condition. The first specimen, referred to as Specimen 1, was cut at location "B" (adjacent to the center gusset plate) as shown in Figure 1. The second was Specimen 2, which was cut at location "A" (mid-length between gusset plates), as indicated in the same figure. These locations were identified through analytical modeling to be the most severe cases in terms of secondary effects in the faulted member. Photographs of torch cuts can be seen in the insets for Figures 8 and 9.

Prior to cutting each specimen to simulate the after-fracture faulted condition, they were loaded in the as-delivered condition over several load cycles to ensure test setup and sensors were operating correctly. Data for the first several load cycles were discarded as part of the "shakedown" of the setup. Shakedown load cycles were performed within the elastic range of the specimen ensuring proper seating of the bolted connections to the load frame. Note that multiple load cycles (or tests) were performed on each specimen to ensure repeatability of results, particularly in the elastic range of loading, each being numbered chronologically as a different test number.

EXPERIMENTAL METHODS

The following sections discuss methods used for experimental research of after-fracture load redistribution behavior of axial steel tension members comprised of two channels. Full-scale laboratory experiments were performed on members removed from a retired bridge taken out of service.

Condition of Test Specimens Removed from Service

The two specimens used for the experimental portion of the research on two-channel members were removed from an approach span of the Winona Bridge that was built in 1940 carrying traffic over the Mississippi River near Winona, Minnesota. Figure 2 shows the general condition of the specimens as they were delivered, after nearly 80 years in service. The condition of the rolled channels was generally sound with minor section loss resulting from corrosion. Figure 2 also shows a sketch of the cross section at one of the stay plates, which has the appearance of a box section; however, the stay plates were intermittent along the lengths spaced at a distance of 43 in. center-to-center (28 in. clear distance). The channels were C15×40 rolled channels, made continuous through the gussets. The cover plates were 14¾ in. tall by ⅜ in. thick and were spliced at the gussets. Moderate to severe pack rust was evident

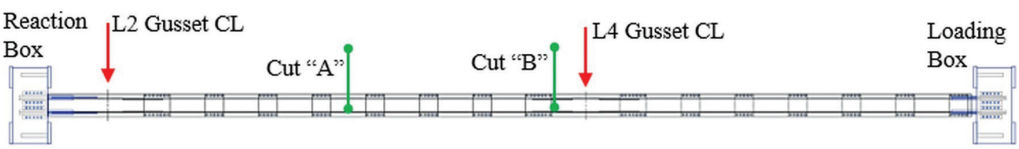

Fig. 1. Plan view sketch of specimen showing locations of the torch cuts.

between the channels and the cover plates along the top of the chords. The gusset connections for the mid-span tension chord sections were also in good condition with some minor corrosion damage. Figure 3 shows a portion of Specimen 2 where cracks were identified in the cover plates resulting from pack rust that were present during all testing. It also shows typical section loss at the stay plates.

Load Frame and Specimen Preparations

A horizontally oriented, self-reacting load frame was designed and fabricated in-house with capacity for 1.5 million pounds. In order to react against the large tension forces, two 60-foot-long W24×146 rolled wide flange beams were used as compression elements in the load frame. Load and reaction boxes (one at each end of the specimen) transferred load between the test specimen and the compression reaction columns of the load frame. Figure 4 shows a specimen placed between the reaction columns with the loading box attached. Figure 5 shows a top-down perspective of this area. The four hydraulic jacks pushed against the loading box, supported by the reaction columns putting the specimen into axial tension. Steel rollers were placed below the specimens and the reaction columns, allowing the entire load frame and specimen to undergo unrestricted strain without impeding their opposing relative displacements.

The two test specimens were removed from a deck truss span of the Winona Bridge, as shown by Figure 6. One came from the east truss line and the other from the west truss line. The specimens were approximately 65 feet long upon arrival and were cut to the final testing length of 740.5 in. (61.7 feet). Rivets were removed at each end and bolt holes were drilled for connection to the loading boxes. All connections were bearing-type connection using 1-in.-diameter ASTM F3125/F3125M Grade A325 high-strength bolts (ASTM, 2019), thereby reducing the number of required bolts. To account for any movement or "shake down" in the connection, load was applied to ensure all connections

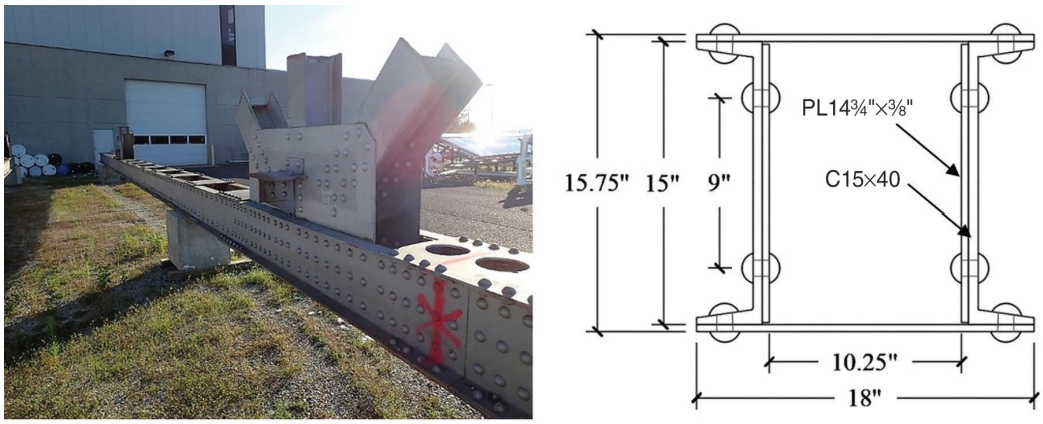

Fig. 2. Winona Bridge specimens.

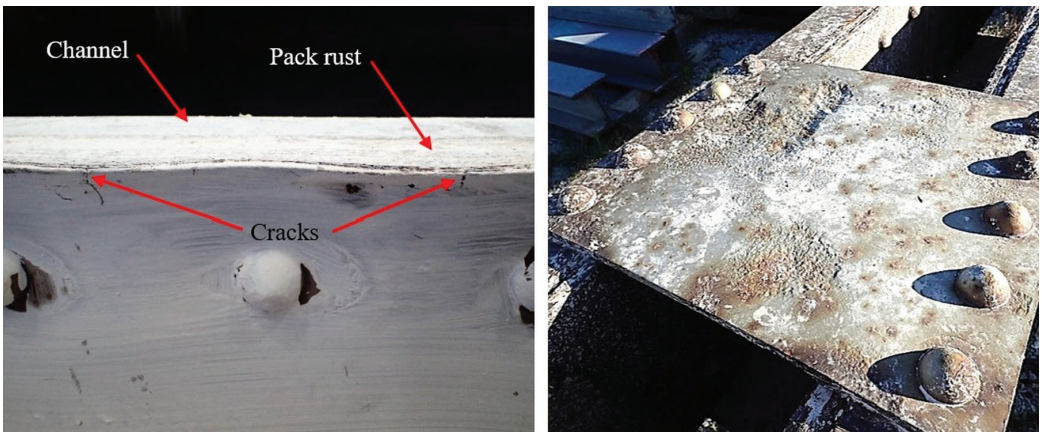

Fig. 3. (Left) Specimen 2 (whitewashed for testing) showing defects and section loss; (right) typical section loss of a stay plate.

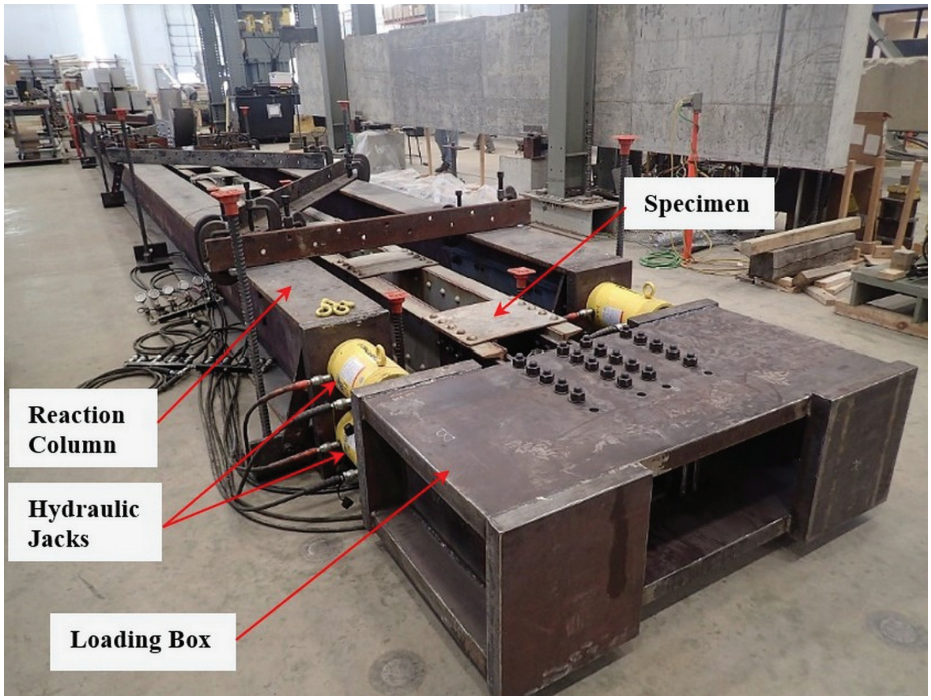

Fig. 4. Load frame with specimen placed and ready for testing.

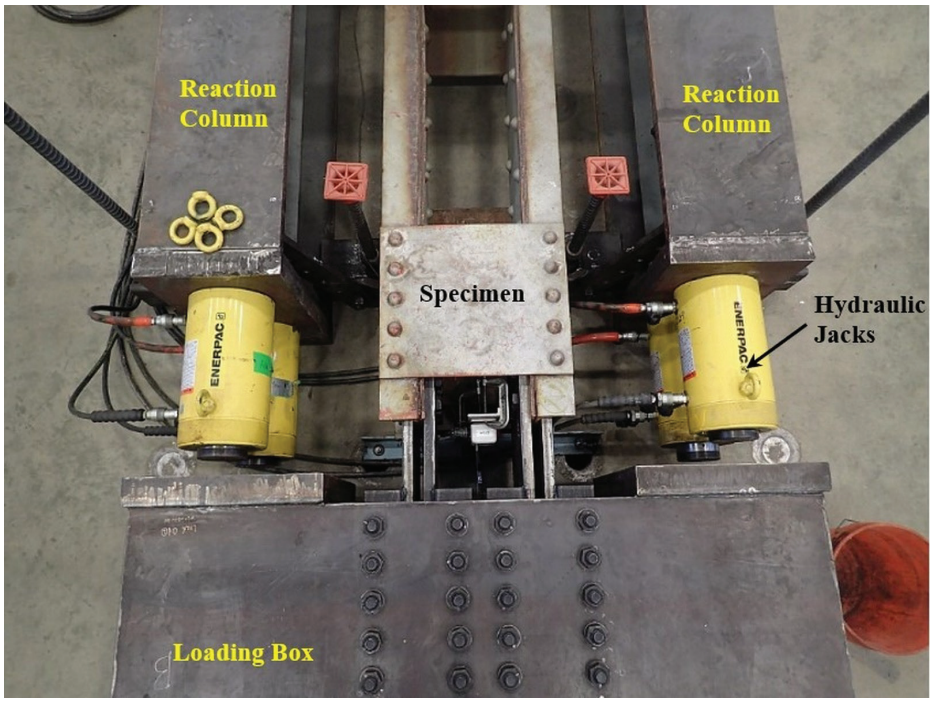

Fig. 5. Top view of loading frame and specimen connection.

Table 1. Comparison of CVN Impact Energy				
Service Temperature (°F)	AASHTO Fracture-Critical (ft-lb)	AASHTO Nonfracture-Critical (ft-lb)	Average for Winona Channel (ft-lb)	Average for Winona Cover Plate (ft-lb)
70 (Zone 1)	25	15	16.0	18.2
40 (Zone 2)	25	15	10.0	10.7
10 (Zone 3)	25	15	6.8	6.0

were fully seated. This process helped remove excess displacements that could be wrongfully attributed to specimen elongation, particularly when the connections are designed as bearing connections and when, inevitably, some of the fasteners go into bearing before others.

Experimental Test Results

The following sections describe the experimental test results, including material testing and static load tests of the specimens in the faulted condition.

Material Testing

Prior to load testing, material samples were removed from the cover plate, channel web, and two gusset plates to test for Charpy V-notch impact (CVN) energy (for estimation of toughness), yield strength, tensile strength, and chemical composition. The material testing was performed according to requirements of ASTM E23 (2016a), ASTM E8 (2016b), and ASTM E415 (2017), respectively. The steel was found to be consistent with the standards of ASTM A7 that likely would have been specified at the time of construction of the Winona Bridge in the late 1930s.

Although some limited chemical specifications and tensile capacity minimums were typically provided in early steel specifications, toughness was not. Toughness is the material property that quantifies the ability of a material to resist fracture in the presence of a notch or crack. Direct measurement of toughness requires costly testing and relatively large piece of material. As a result, an economical alternative often used is the CVN test. These tests are not a direct measure of toughness, but rather a measure of energy absorption. However, using accepted correlation methods, such as the master curve method, fracture toughness can be estimated from CVN data. Table 1 compares the modern CVN impact energy requirements from Section 6 of the *AASHTO LRFD Bridge Design Specification* (AASHTO, 2020) with the average of three CVN impact energy test results at the service temperature indicated. As a point of interest, the only category for which the historic steel would meet the modern specification is Zone 1 Nonfracture-critical. See the complete results of the material tests provided by Lloyd et al. (2019).

Load Test Results

Figure 7 shows a load-displacement plot for Specimen 1 prior to being purposefully cut to simulate a partial member failure. The line labeled "Nominal" is the calculated, or nominal, load-displacement curve based on a simple mechanics of materials equation for displacement of an axially loaded body (i.e., $\delta = PL/AE$) using the gross cross-sectional area. The measured load-displacement relationship correlated well with the nominal estimation and indicated a linear-elastic response to the applied load. The peak load of 1150 kips surpassed the original design load for the member by 222% and effectively reached the upper bound capacity of the hydraulic jacks. This portion of the testing helped confirm proper loading and unloading cycles were being performed and that sensors were operating as desired. Next, load was removed and Specimen 1 was cut between the end stay plate and the L4 (center) gusset plate

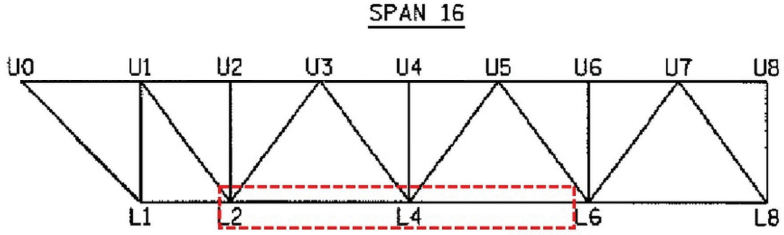

Fig. 6. Winona Bridge deck truss span—specimens removed from area shown by the dashed line.

(location "B" as indicated on Figure 1) leaving only half of the original cross section intact. Several load cycles were applied to the member in this condition, including a final load cycle up to 800 kips, as plotted in Figure 8. The calculated, or nominal, load-displacement curve has also been plotted and labeled for the linear-elastic portion of the loading, which does not take into account the loss of half the cross section. In other words, the full cross-sectional area was used in the nominal estimate. The nominal, or unfaulted, member stiffness is used in this case to make a comparison back to Figure 7, demonstrating the change in stiffness as a result of the simulated fracture. The curve is based on the simple calculation of elastic displacement of an axially loaded body, as explained earlier. However, in this case, it is not an equitable comparison because the measured curve now represents the member in the faulted condition with only half of its cross section at location "B" (i.e., near the gusset plate). The specimen experienced approximately an 18% reduction in axial stiffness in the faulted condition. This is without the benefit of system behavior one might expect for a member in a bridge where other members, bracing, etc., are connected to the faulted chord provided alternative load paths and additional stiffness. That is to say that in a real-world application, any loss of axial stiffness in the faulted member would result in the member shedding some load to adjacent members. System behavior was observed by Diggelmann et al. (2013) during field testing of a deck truss bridge where explosives were used to sever half of a built-up channel member on the Milton-Madison Bridge. The load measured in cross members, as well as in the truss line opposite the severed member, were observed to increase slightly. This is an important observation simply because all evaluation methods developed in this research conservatively assume that the entire load originally carried by the faulted member remains in the faulted member. However, minor load shed from the damaged member will help improve both strength and fatigue performance of a member in the faulted condition in real-world conditions.

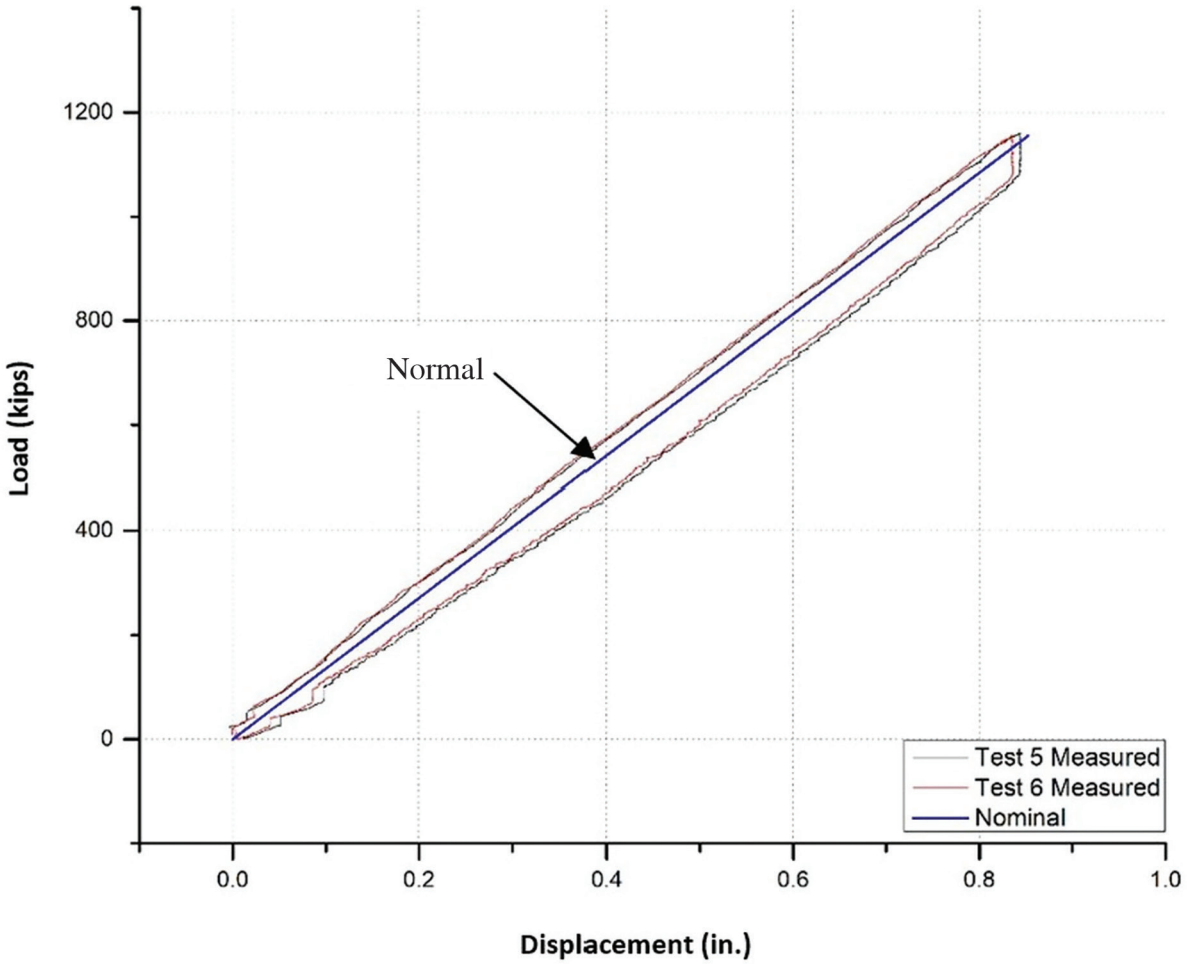

Fig. 7. Load vs. displacement curve for Specimen 1 prior to severing half of the cross section showing predictable elastic behavior.

Table 2. Test Specimen Cross-Sectional Area and Capacity in the Faulted Condition		
	Specimen 1 (at Location "B")	Specimen 2 (at Location "A")
Faulted gross area (in.^{2})	19.2	17.3
Faulted net area (in.^{2})	15.9	14.5
Nominal load at gross section yield (kips)	632	571
Predicted load at gross section yield (kips)	754	679
Nominal load at net section fracture (kips)	954	870
Predicted load at net section fracture (kips)	1070	972
Maximum test load (kips)	800	647

Table 2 provides the "nominal" (based on published ASTM A7 material properties) and "predicted" (based on measured material properties) section capacity calculations for the specimen in the faulted state. Figure 8 plots results for Tests 12 (elastic range) and 13 (failure). It can be seen in Figure 8 that the onset of yielding occurred during Test 13 at around 600 kips, which is notably less than the predicted gross section yield load on the faulted section of 754 kips. However, a yield load based on the faulted *net* section is approximately 625 kips. The initial onset of yielding probably began at the fastener holes, most likely the first set of rivets shared by the splice plate and cover plate or gusset plate. This is supported by the locations of observed rivet slip in the final load cycle for Specimen 1 (see Figure 10). At the peak load, it can be observed that the specimen began inelastic deformation holding peak load momentarily through minor strain hardening before permanent deformation increased and began to shed load.

Note that the faulted specimen exceeded the original design load of 517 kips (obtained from the original design drawings) by 15–20% before the onset of yielding and was able to reach about 1.5 times the design load before onset of gross section yielding on the faulted section. This is remarkable considering that the specimen reached this load while also resisting flexural stress resulting from an after-fracture second-order moment at the location of the failure.

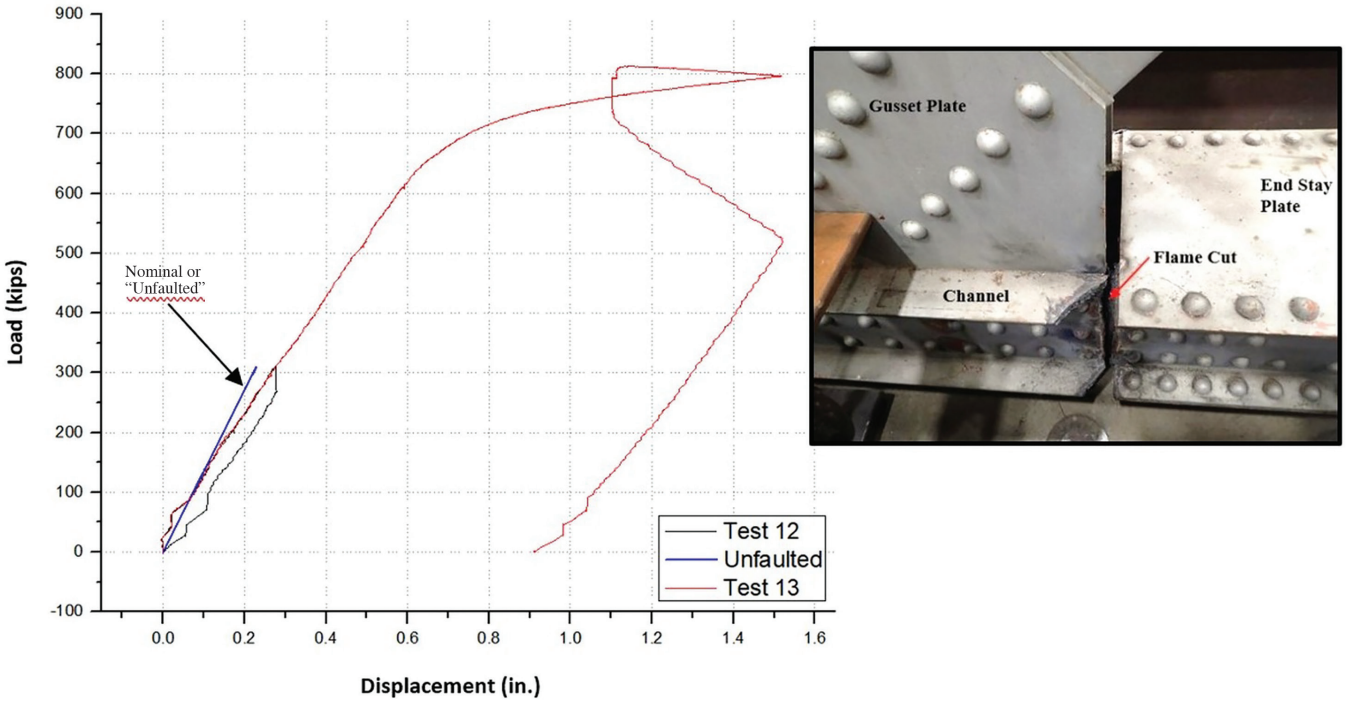

Fig. 8. Load vs. displacement curve for Specimen 1 (cut near gusset plate).

Specimen 2 was also loaded several times in the unfaulted condition in order to perform a shakedown on the connections and ensure the specimen was seated into the load frame properly. Several additional static load cycles were applied on the faulted section up to a peak load of 647 kips. A few of these have been plotted in Figure 9 where cycles up to 300 kips remained linear-elastic and later cycles reaching loads of 600 kips or more produced permanent plastic deformation on the faulted section. The calculated nominal load-displacement curve of the member in the unfaulted condition has also been plotted as reference. In this case, the axial stiffness of the specimen in the faulted condition was reduced by 45% (within the elastic range of loading). This would have resulted in load shed to adjoined members in an actual structure. This is notably more loss as compared to Specimen 1, likely due to the fact that Specimen 1 had the benefit of mutiple members and plates within the vicinity of the failure (cross-member stubs connecting gusset plates, bracing, etc.) helping to provide stiffness and load transfer. Table 2 provides the "nominal" (based on published A7 material properties) and "predicted" (based on measured material properties) section capacity calculations for the specimen in the faulted state. Similar to Specimen 1, Specimen 2 experienced what was likely a net section yielding at about 500 to 550 kips, which is less than the calculated gross section yielding load of 679 kips. The 550 kip load closely corresponded with a yield load calculated on the *faulted* net section of 565 kips. Once again, the faulted specimen was able to achieve loads in excess of the original design load (obtained from design drawings)—in this case, by just over 25%—in addition to resisting the after-fracture second order-moments induced by resdistribution of loads around the failure.

In both cases, the stay plates showed no sign of permanent deformation at the peak loads. Figure 10 shows Specimen 1 after testing has been completed where localized damage is labeled, such as channel flange buckling, slip at the rivets, and rotation of the end stay plate. Slip at the rivets indicates that either the rivet has yielded, the plate has yielded locally at the rivet hole, or both. The in-plane rotation of the stay plate shown in the figure was indicated at the corner of the end stay plate where a small unpainted section of the channel was exposed. The stay plates resisted opening of the severed channel through horizontal in-plane shear action. This put part of the stay plate in tension and part of the plate in compression, the capacity of which would theoretically be controlled by the buckling capacity of the plate. However, in both experimental cases, and as was later confirmed in the parametric study, the faulted member capacity was not limited by the stay plate thickness (and thus buckling capacity), which was found to have no effect on the internal redundancy analysis. The plates for

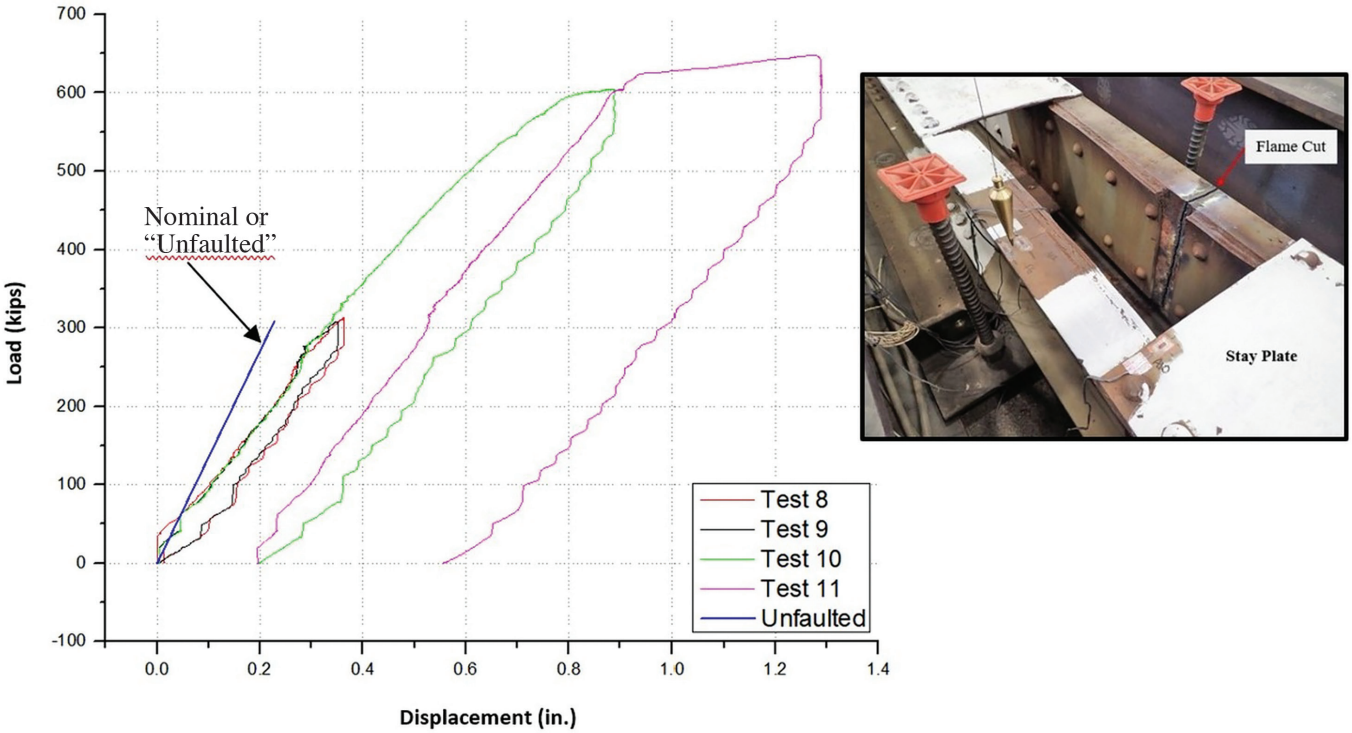

Fig. 9. Specimen 2 load-displacement curves (cut at mid-panel).

Specimen 1 and 2 were ⅜ in. thick—a common thickness for riveted built-up members and which can be considered a typical minimum thickness for stay plates.

PARAMETRIC STUDY OF TWO-CHANNEL MEMBERS

Global behavior of two-channel members resulting from a single failed channel was investigated in a parametric study using the Abaqus software suite. The parametric study resulted in several simplified solutions intended to be used to calculate second order moments, which can be superimposed to estimate the live load stress range in the unbroken channel.

Two-Channel Member FEM Calibration and Specifications

Finite element models for the two-channel member parametric study were calibrated using the experimental test data from Specimen 1 and 2. Following FEM calibration, numerous three-dimensional member geometries were created and evaluated using linear elastic, static implicit analysis. The geometries studied included stay-plated members and double-latticed members with the intersection of the lattice bars connected. Single lattice bar configurations were not studied after research showed that lacing bars contribute negligibly to load redistribution in the faulted condition. This is discussed in greater detail below. Concentrated loads were applied at reference points that were connected to the member cross section using kinematic coupling constraints, which uniformly distributed the load. Plates and channels were modeled using four-node doubly curved shell elements with reduced integration and hourglass control (Abaqus designation S4R) and a structured quadrilateral mesh. The global mesh size was ½ in. using the Simpson integration rule with five integration points through the thickness of the shells. Lattice bars were modeled using two-node linear beam elements (Abaqus designation B31) with a 1½ in. mesh size. A shell element mesh convergence study was performed halving the mesh density to 1 in. elements and then doubling the mesh density to ¼ in. elements at locations adjacent to the failure sites. It was found that the results were insensitive to the mesh size up to at least 1 in. However, the ½ in. element size facilitated the integration of nodal forces at locations of interest without significant increase in computational cost.

Figure 11 is zoomed in on a gusset plate connection on the +60-ft-long specimen showing a typical mesh for the models. Rivets were not explicitly modeled. Although nonlinear connector elements were initially used that were calibrated to experimental single fastener shear test data obtained from Ocel (2013), no significant improvement to the stress outcomes was observed. Hence, the use of connector elements to model rivets was not carried forward into the parametric study. Instead, plates and channels were connected using surface-to-surface tie constraints. Lattice bars were connected to channel flanges and at center points of lattice bar intersections using kinematic tie coupling constraints that allowed rotation about what would be the fastener longitudinal axis.

For the benchmark FEM, an elastic-plastic isotropic material was defined for the channels and plates having a yield strength equal to the measured cover plate yield strength of Specimen 1 and 2. The modulus of elasticity was defined as 29,000 ksi and a Poisson's ratio of 0.3. Following calibration of the shell element models, the material definition was simplified to linear-elastic for the parametric study.

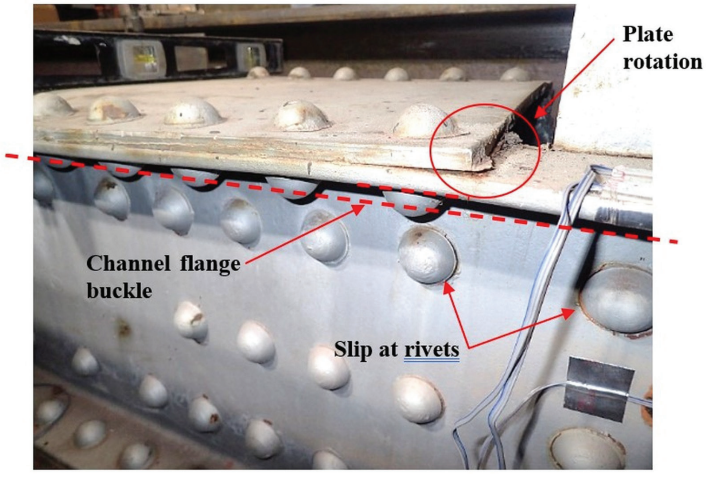

Fig. 10. Specimen 1 after testing showing signs of permanent deformation.

Data collected during the laboratory testing of Specimens 1 and 2 were compared to the benchmark finite element model to calibrate the model parameters and ensure accurate solutions. Strain, load, and displacement sensors used during the experimental testing provided data for comparison. Figures 12 and 13 show load-displacement curves for each of the specimens compared to load-displacement results obtained from the benchmark FEM. While the load-displacement relationship was not necessarily the output of interest for purposes of the parametric study, it was considered a useful indicator of overall behavior and response to load in comparison of the laboratory test results to the FEM results—particularly in the faulted condition.

Figure 12 plots data for Specimen 2, where the member was cut at location "A" (midpoint between gusset plates). Several elastic load cycles were applied, followed by two large load cycles resulting in permanent plastic deformation. It can be seen in Figure 12 that the FEM results compared relatively well with the laboratory results, particularly within the linear-elastic range up to about 400 kips. The FEM load-displacement curve showed reasonable nonlinear behavior, as well. The same can be said for Figure 13 comparing FEM results to Specimen 1, which was cut at location "B" (between the gusset plate and end stay plate). The goal of this benchmarking process was to simplify the FEM as much as possible while achieving reasonable and acceptable accuracy that could be carried forward into the parametric study. The lack of undue complexity of the model resulted in the divergence at peak loads seen in the plots. For example, at peak load, slip at rivets immediately adjacent to the failure site, slip at bolted connections used to attach the specimen to the load frame, in-plane rotational slip of the stay plate pairs closest to the failure site, as well as localized fastener hole deformation at extreme loads were observed. These sources of additional axial displacement would not be captured by the simplified FEM but were not considered necessary for the objectives of the parametric study either, which focused on linear-elastic behavior in the faulted condition that would be used for fatigue-based stress-range calculations and subsequent fatigue life estimates.

Strain gages were placed at several cross sections along the length of the test specimens. The benchmark FEM longitudinal stress results were within 10% or less of laboratory results at all critical areas, such as near the points of severed members, and within 15% or better at all other locations. Figure 14(a) shows a cross-sectional view of the benchmark FEM at the site of the "failure" of Specimen 2. Symbols are sketched at approximate locations where the strain gages were installed, corresponding to the stress plots in Figures 14(b)–(d). Figures 14(b)–(d) plot stress on the vertical axes and transverse position on the component on the horizontal axes. Dashed lines are also sketched on Figure 14(a), corresponding to the path across which the stress outputs were obtained from the FEM. Figure 14(b) shows longitudinal normal stress across the width of the cover plate. The triangle indicates the location of the strain gage, which was centered between the edges of the cover plate, as well as between the adjacent stay plates, directly across from the severed half of the member. Figure 14(c) shows longitudinal normal stress across the width of the channel flange. Two strain gages were installed on the flange: One (diamond) was located 1½ in. from the edge of the flange, and the other (circle) was ½ in. from the edge. Both of these gages were centered between the adjacent stay plates directly

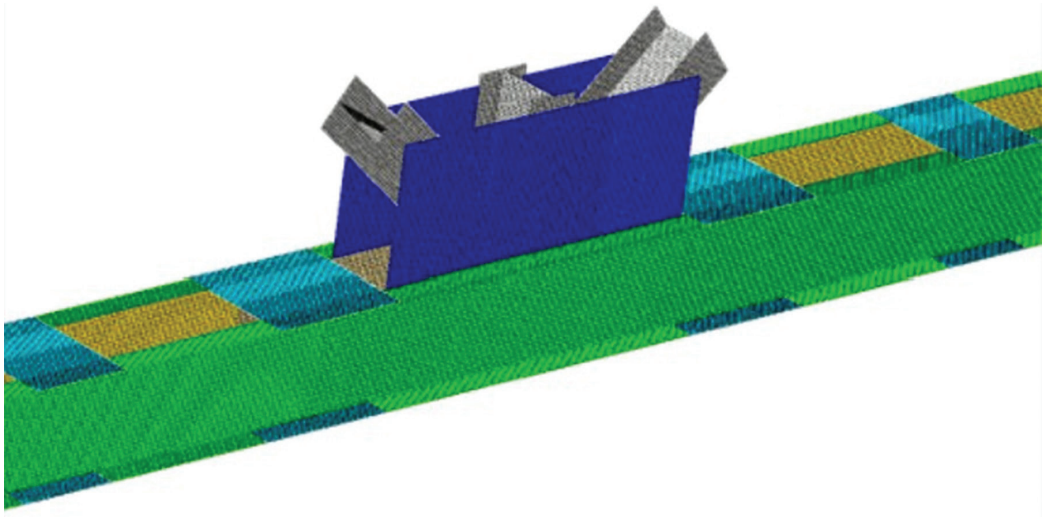

Fig. 11. Typical ½ in. shell element mesh used for FEM validation and two-channel member parametric study.

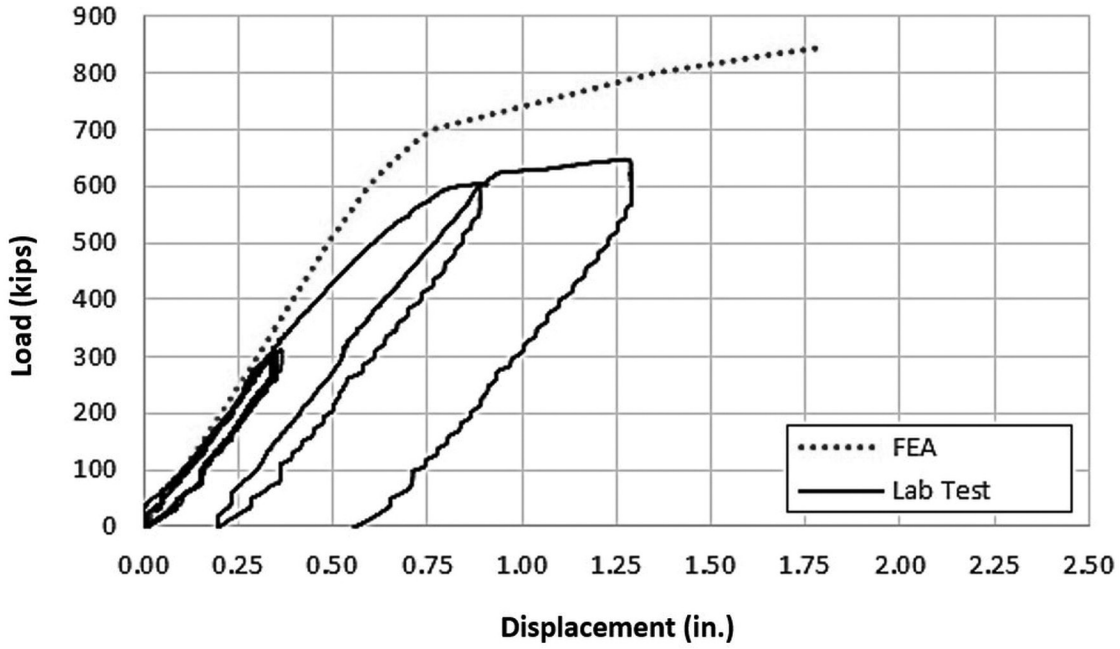

Fig. 12. Benchmark data comparing FEA results to lab test data for Specimen 2 in faulted condition with severed member at mid-panel (Cut "A", Fig. 1).

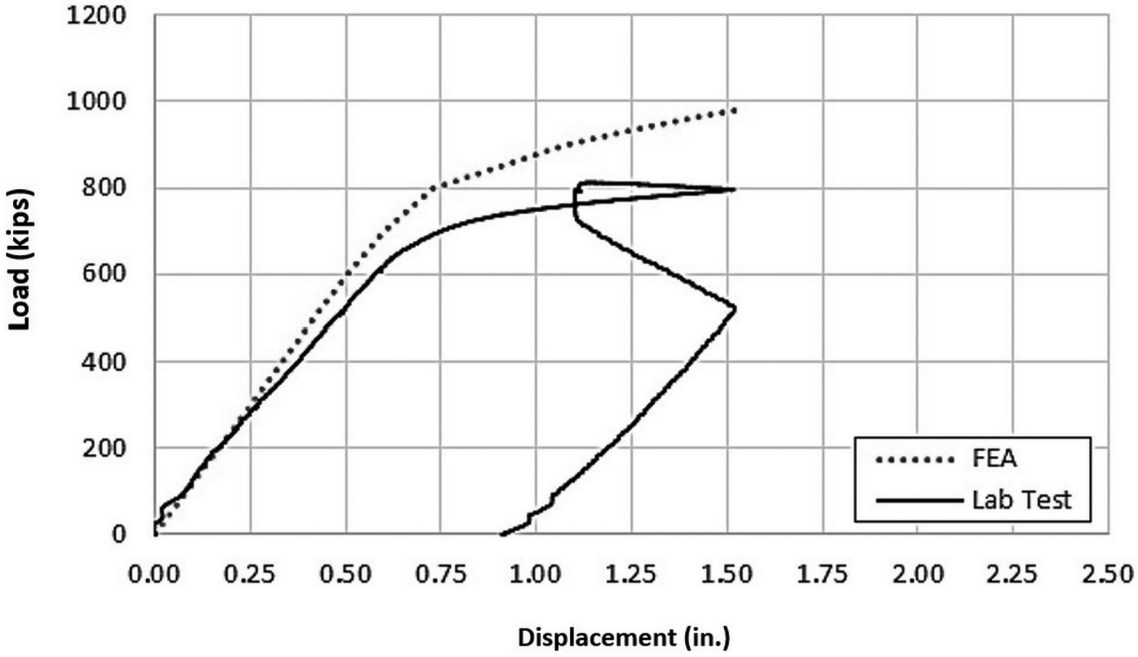

Fig. 13. Benchmark data comparing FEA results to lab test data for Specimen 1 in faulted condition with severed member at mid-panel (Cut "B", Fig. 1.)

across from the severed half of the member. Figure 14(d) plots longitudinal normal stress across the width of the channel web. The square indicates the location of the strain gage, which was directly opposite the strain gage installed at mid-depth on the cover plate. The applied load was 300 kips. All FEM results in this location were within 10% or less of laboratory measurements.

Figure 15 shows a rotated elevation view of the same FEM, where the severed half can be seen, along with the stress hotspots at the corners of the stay plates. The strain gage symbols have also been placed on Figure 15 to illustrate their approximate positions. Note that the cover plate gage (triangle) is out of view. Stresses in the intact half of the member resulted from the axial load applied to the member, as well as a secondary moment resulting from load redistribution around the discontinuity. Stay plates functioned as load paths for the redistribution, carrying load through in-plane shear and helping resist opening of the severed half of the member. This caused the intact member to displace inward (toward the severed member). Out-of-plane displacements of the FEM at the location of "failure" matched laboratory specimen measurements to within 5% at peak loads.

Pinned and fixed boundary conditions were also applied to the FEM to understand the effect it may have on the benchmark results. It was found that end boundary conditions had a negligible effect likely due to benefits attributed to the member being continuous at the center gusset, meaning more than a single panel length. The influence of boundary conditions within the context of the parametric study is discussed in more detail later.

The benchmark shell element model, as described herein, was found to be acceptably accurate, particularly within the linear-elastic range. Stresses and displacements outputs at locations of highest interest were found to be within 10% of that measured in the laboratory tests and therefore, set the standard for finite element models used in the parametric study.

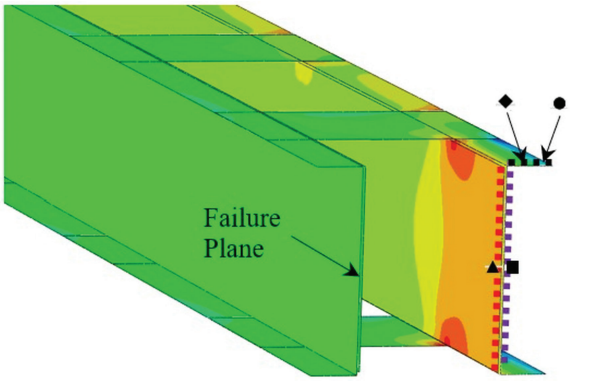

(a) Isometric view of the FEM identifying the approximate locations of the sensors

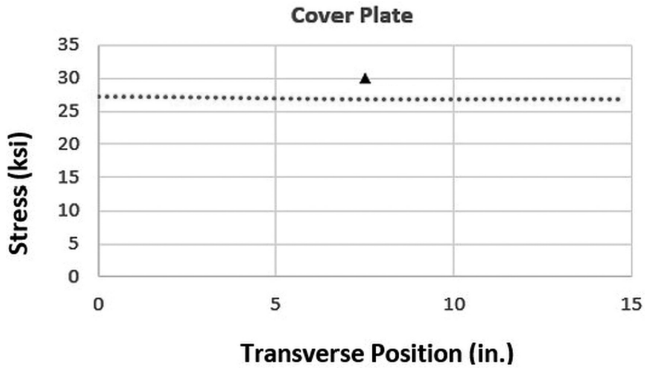

(b) FEA vs. measured stress at inside cover plate surface [see Fig. 14(a)]

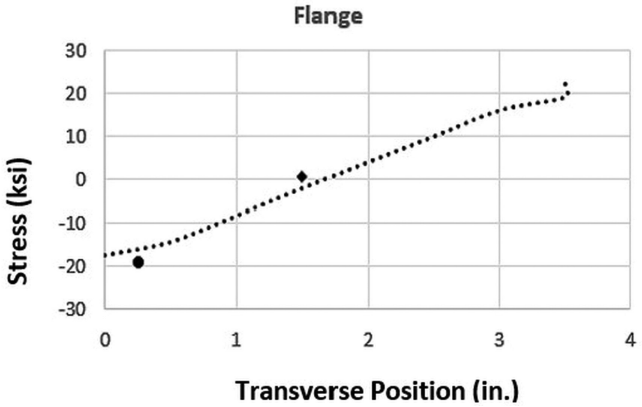

(c) FEA vs. measured stress at top of channel flange surface [see Fig. 14(a)]

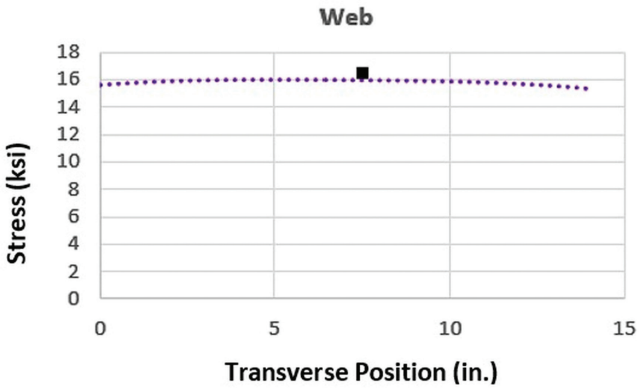

(d) FEA vs. measured stress at inside channel web surface [see Fig. 14(a)]

Fig. 14. Benchmark data comparing FEA results to measured data at the location of failure.

Geometric Parameters Varied for Two-Channel Members

The parametric study was divided into four subgroups: continuous stay-plated, continuous laced, noncontinuous stay-plated, and noncontinuous laced. Continuous stay-plated members are two-channel members where the channels are connected using intermittent stay plates (also known as batten plates) and made continuous through multiple panel points (or truss nodes). Continuous laced members are two-channel members with the channels connected using lattice bars and made continuous through multiple panel points. The noncontinuous stay-plated members are two-channel members connected using intermittent stay plates and extending between two panel points, such as would be the case for a truss shear diagonal member. The noncontinuous laced members are the same as noncontinuous stay-plated members, except that the channels are connected using lattice bars instead of stay plates. Each of these subgroups was studied for effects of equivalent applicable parameters but were divided into subgroups due to the differences in after-fracture load redistribution behavior.

The modern AASHTO *LRFD Bridge Design Specification* (AASHTO, 2020) is silent on the sizing and spacing of stay plates and lattice bars for built-up tension members. It does provide guidance on the design of built-up compression members, including single-angle members. Many existing built-up members, however, were constructed long before the modern LRFD design specifications. The earliest AASHTO design specification that could be referenced for this work was *The Standard Specifications for Highway Bridges* adopted by AASHO (now AASHTO) in 1935 (AASHO, 1935). It provided design guidance for built-up tension and compression members. It states that separate segments of tension members composed of shapes may be connected by stay plates or end stay plates and lacing. End stay plates for tension members were required to be sized the same as for compression member intermediate stay plates. Intermediate stay plates of tension members were required to be sized at a minimum of three-quarters of that specified for compression member intermediate stay plates. Additional information on the design provisions of stay plates from AASHO 1935 is summarized by Lloyd et al. (2019).

The *AREMA Manual for Railway Engineering*, Chapter 15, provides guidance on design of stay plates and lattice, as well (AREMA, 2017). It states that built-up members shall be connected by stay plates or lacing bars with end stay plates. It goes on to specify that tension members shall have stay plates sized to a minimum of two-thirds the lengths specified for stay plates on primary compression members. The angle of orientation of lacing bars, thickness of the lacing bars, and fastener requirements was found to be similar to the requirements of the 1935 AASHO Standard Specifications. Additional information on the design provisions of stay plates and lattice from AREMA is summarized by Lloyd et al. (2019). It was preferred to develop a simplified method of analysis that would be inclusive of all reasonable designs, including those that were designed per the 1935 AASHO provisions and those designed per the AREMA provisions. Therefore, the parametric study included a range of models with size and dimensional aspects that enveloped the requirements of the 1935 AASHO *Standard Specifications* (AASHO, 1935).

Parameters Evaluated for Two-Channel Members

Lloyd et al. (2019) provide details as to the geometries considered in that parametric study within an appendix. The reader is encouraged to reference that report for more information. Many of the parameters evaluated for the two main types of members, stay-plated and laced, were similar. However, there were several parameters unique to each type of two-channel member. The parameters evaluated for stay-plated members included:

- Boundary conditions: Fixed vs. pinned
- Channel section: C8×11.5, C15×40, and C15×50
- Channel spacing: From ½ channel depth to 2 times channel depth

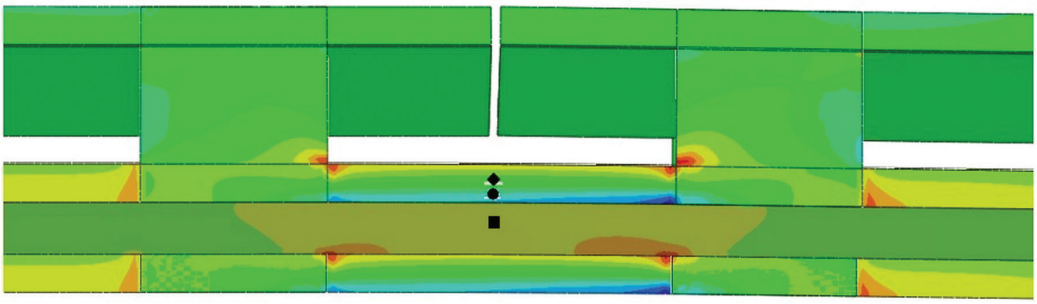

Fig. 15. Benchmark FEM showing location of the severed half and stress hotspots at load equal to 300 kips.

- Panel length—referring to the distance between two adjacent gusset joint centerlines: From 20 to 40 ft
- Stay plate thickness: From ⅜ to ⅞ in.
- Stay plate length: From ½ channel depth to 2 times channel depth
- Stay plate clear spacing: From 18 to 148 in.
- Gusset plate thickness (for noncontinuous only): From ⅜ to ⅞ in.
- Location of failures: Next to the gusset vs. centered between gussets at mid-panel

The laced members were always modeled with end stay plates. Based on results for the stay-plated members, the thickness and length parameters of the end stay plates were not varied. Additionally, results for the stay-plated members also showed that gusset plate thickness for the noncontinuous members had negligible effect and therefore was not varied for the laced members. The parameters considered for laced members included:

- Boundary conditions: Fixed vs. pinned
- Channel spacing: From ½ channel depth to 2 times channel depth
- Panel length—referring to the distance between two adjacent gusset joint centerlines: From 20 to 40 ft
- Lacing bar thickness: From ⅛ to ¾ in.
- Lacing bar length: Dependent on lacing bar spacing and channel spacing
- Lacing bar spacing—referring to the distance between connecting rivets to the channel flange, which determined the lacing angle relative to the channel: From ½ channel depth to 2 times channel depth
- Location of failures: Next to the gusset vs. centered between gussets at mid-panel

Boundary conditions were found to have a significant effect on results for noncontinuous members, which is discussed in greater detail later. Three sizes of rolled channels were considered; however, not all sections were considered for all combinations of parameters. They are sketched to scale in Figure 16 to give a sense of relative sizes. C15×50 is the largest rolled channel section currently available, so it was selected to learn if parametric effects varied between it and the next size smaller. C15×40 was chosen because in the authors' experience, it is the most commonly used rolled channel section for tension elements in legacy bridges. It is noted that a C15×40 was used to construct the Winona Bridge from which the two test specimens were obtained for the present research. The C8×11.5 was selected as a channel that is most likely representative of the smallest useable size channel for bridges. While this size channel probably would not be found on railroad bridges, it could be

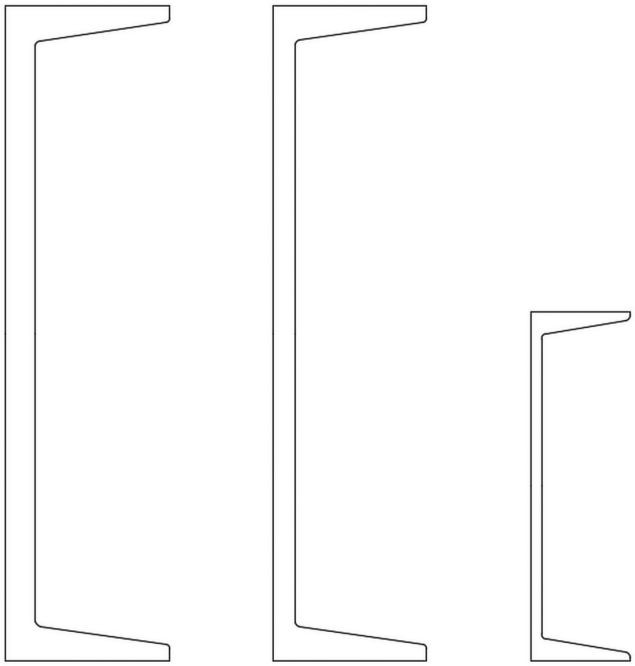

Fig. 16. Channel sections included in the parametric study.

possible for short span highway bridges as shear diagonals or hangers.

Gusset plates were modeled for the noncontinuous members, as discussed later. The thickness of the gusset plates was modeled as ⅜ and ⅞ in. to bound the limits of typical gusset plate thickness. The location of the failure within a member was also examined for the effect on results. Two locations were studied for all geometries, which included one at the mid-panel location centered between the gusset connections, and the other was adjacent to gusset plates located between the end stay plate and the gusset connection, thereby conservatively removing the benefit of the stay plate. This was considered for the continuous, as well as the noncontinuous types.

Definition of Eccentricity Parameter, **e**

Figure 17 illustrates the dimension "*e*" used in the post processing of data from the parametric study. 2*e* represents the distance between the centroids of individual channels that make up a two-channel member cross section. For the purposes of this paper, *2e* is referred to as the "channel spacing." Hence, *e* is the distance from the unfaulted *member centroid* to the centroid of an individual channel within that cross section. The figure further illustrates how 2*e* for two members that are comprised of the same size of channels with the same web-to-web spacing, but in reversed orientation, may differ from each other. The parametric study included some channels in both orientations. All results discussed in the following used the appropriate nominal moment, *Pe*, to normalize the second order moment resulting from failure of a single channel; where *P* is the total load in the member. In this way, a simplified method to calculate the resulting after-fracture, secondary moments in two-channel members as a percentage of *Pe* was developed.

Rotational Stiffness of Joints for Continuous and Noncontinuous Two-Channel Members

End boundary conditions were the most influential parameter affecting the resulting second-order moments in noncontinuous two-channel members in the faulted condition. The applied end boundary conditions were effectively inconsequential for continuous members due to rotational stiffness provided by the continuity of the channels. Varying boundary conditions were modeled for each geometry, including a noncontinuous member with pinned ends, a noncontinuous member with fixed ends, a three-span continuous member with pinned ends, and a three-span continuous member with fixed ends. It was observed that the percent *Pe* for the noncontinuous member with pinned boundary conditions differed as much as 10 times more than the same geometry with fixed boundaries. Continuous members had similar results to fixed noncontinuous members and were found to be insensitive to end boundary conditions. Continuity of the channels through the panel points provided rotational constraint that approached fixed boundary conditions. No additional rotational constraints were added at the interior panel points of the three-span members. However, they did have displacement constraints simulating bracing points of connection that would exist on an actual bridge to prevent out-of-plane displacement.

Primary and secondary members—including chords, floor beams, diagonals, lateral braces, sway braces, and bearings—tie into panel points on a truss that are typically connected using gusset plates. Chords or diagonal members will contribute some level of restraint for the joint against rotation (in all three axes and against torsion), particularly under tension. Other members such as lateral bracing and sway bracing may also help to restrain against rotation of the gusset connection. Floor beams, often with full-depth connections, increase rotational constraint of the connection. In some cases, fixed bearings, or even guided expansion bearings designed to only displace longitudinally, could offer further resistance to rotation for the gusset connections at supports. The combined restraint provided by all these members is difficult to estimate without finite element analysis of each individual bridge and member geometry, which would not be feasible for most bridge owners, nor was it the desired outcome of this research. However, the potential for there to be an effect of the rotational stiffness

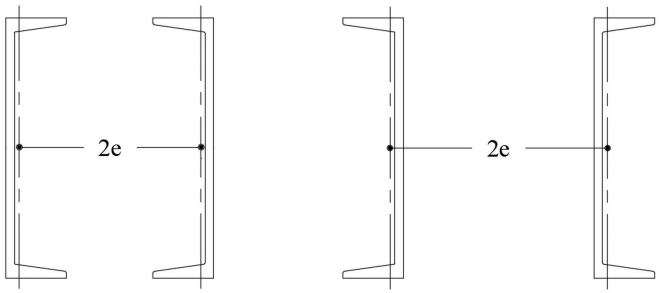

*Fig. 17. Illustrations showing eccentricity "*e*" used in development of the simplified evaluation method for two-channel members.*

on the after-fracture behavior of two-channel members was obvious. It was clear that pinned conditions would not exist in actual bridges. However, it would be problematic to justify perfectly fixed conditions, as well.

Consider further that diagonal and vertical two-channel members are usually "deeply" connected into gusset plates; often they would be trimmed such that they fit tightly into the connection to within a few inches of the other intersecting primary members. An example of this is shown in Figure 18, which shows a removed railroad deck truss joint with diagonal two-channel members connected into the gusset plates to within a couple inches of the continuous tension chord. Due to the rotational stiffness of the connection for reasons previously stated, it was suspected that most rotation experienced by a two-channel member would likely be due to local flexure of the gusset plates near or at the edges of the gusset plates. The plates themselves would behave as fixed toward the center of the connection. Thus, the concept was modeled by tying the channels to a set of gusset plates and then applying fixed boundary conditions to the free edges of the gusset plates. In this way, generous flexibility of the gusset plate was allowed while simultaneously providing a reasonable level of rigidity at the edge of the gusset plate modeling the interaction of intersecting members within the joint.

A pilot parametric study was carried out to determine how best to model the end boundary conditions of the noncontinuous members without overestimating joint rotational stiffness. The parameters considered in the pilot study included the effective portion of the gusset plate, the member embedment depth into the gusset plate, the gusset length beyond the member, and the gusset plate thickness. Figure 19 shows an illustration of these parameters. Two different effective areas of gusset were examined: a simple rectangular shape shown on the left and a Whitmore section-like shape shown on the right. The member embedment depth was evaluated looking at depths ranging from half the channel depth to two times the channel depth. The gusset plate length beyond the member, labeled *L* on the figure, also ranged from half the channel depth up to two times the channel depth.

Figure 20 plots the results of the rotational stiffness parametric study. Green dots represent values resulting from mid-panel failures. Black dots represent values resulting from failures near the gusset connections, such as those labeled in Figure 19. The rectangular and Whitmore-like effective gusset plate shapes are both represented in the data. The chart on the left plots the percent of *Pe* on the vertical axis and the member embedment depth into the gusset plate, normalized by the channel depth, on the horizontal axis. The chart on the right plots the same vertical axis and the gusset plate length, *L*, on the horizontal axis. By quadrupling the embedment depth, the percent *Pe* only increased by 2% for failures near the gusset plate and by less than 1% for mid-panel failures. By quadrupling the gusset plate length, *L*, the percent *Pe* increased by less than 1% for both failure locations. The final parameter considered was the thickness of the gusset plates. ⅜-in.-thick gusset plates are the thinnest plates used in bridges. The thickest plate is unknown. Several noncontinuous models were analyzed

Fig. 18. Example of deeply set diagonal members connected into a gusset plate.

varying only the gusset plate thickness from ⅜ in. to ⅞ in. It was found that results differed by 3% or less.

The rotational stiffness study concluded that outcomes were insensitive to the shape of the gusset assumed to be engaging in rotational constraint, the member embedment depth, the gusset plate length *L*, and the gusset plate thickness. As a result, noncontinuous FEMs were modeled in the primary parametric study using ⅜-in.-thick rectangular gusset plates with embedment depths and gusset plate lengths equal to the channel depth.

Finally, when percent *Pe* results shown in Figure 20 were compared back to previous model results with varying end boundary conditions, it was observed that by adding the gusset plates to the noncontinuous members, percent *Pe* fell between results for pinned and fixed boundary conditions, more closely resembling that of fixed boundary conditions and comparable to the continuous members. It is believed that this method of analysis reasonably and conservatively simulates typical boundary conditions on actual bridges for the noncontinuous two-channel members, which has a significant effect on the internal redundancy evaluation.

Results for Parametric Study of Two-Channel Members

The largest resulting second-order moments were always located in the intact member directly across from the location of failure. The largest of these moments nearly always resulted from a failure between the gusset plate and end stay plate, particularly for stay-plated members. Figure 21 shows the plan view of several FEMs with exaggerated deflections to illustrate general behavior. Two failed at the mid-panel, (a) and (b), and two failed between the gusset plate and end stay plate, (c) and (d). Overall global behavior was relatively

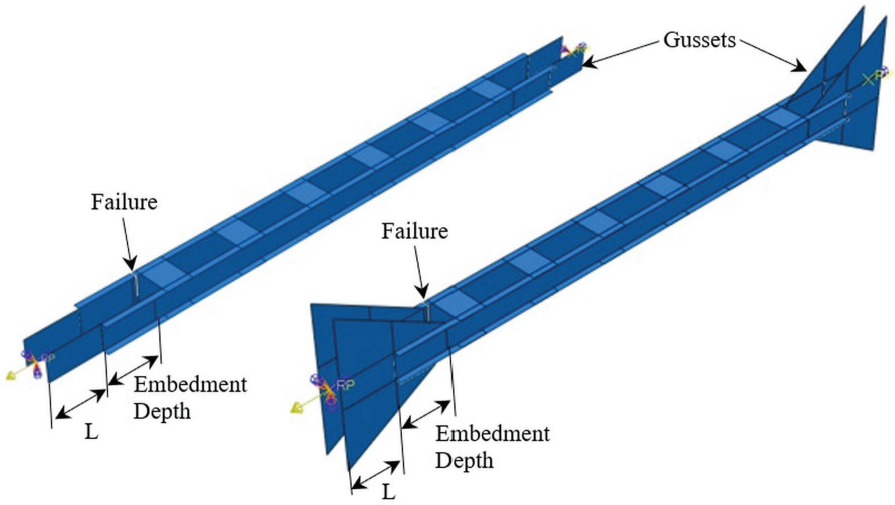

Fig. 19. Example of FEMs used to study gusset connection parameters: (left) rectangular gusset; (right) Whitmore gusset.

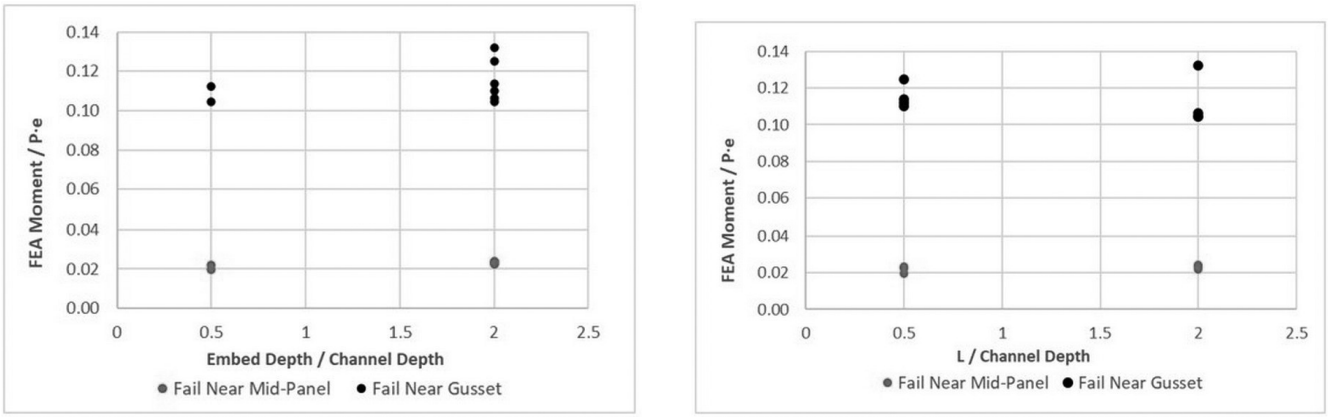

Fig. 20. Effects of the member embedment length (left) and gusset length, L (right).

similar between these two member types when they had failures at the same location. Mid-panel failures allowed moment distribution along the length of the intact channel via lattice bars or stay plates helping to distribute load more gradually around the failure. Gusset-end stay plate failures, however, forced much of the resulting moment to be resisted within a more localized area. Deflections across the remainder of the member were relatively gradual, as can be seen in Figure 21(c) and (d).

Moments integrated at the mid-panel of members with gusset-end stay plate failures were found to be very small compared to moments at the end stay plate near the failure. Stay-plated members were also observed to experience localized reverse curvature at the edges of the stay plates that produced hot spots of stress and amplified moments, as shown amplified in Figure 22. All moments reported in the following sections were taken near the edges of stay plates, when applicable, to capture the largest resultant moment. The opening of the fracture plane was resisted through in-plane shear in the stay plates. Laced members also benefited from in-plane shear resistance provided by end stay plates.

The size of the channel was found to have a negligible effect on outcomes. This makes sense when considering that loads were proportioned to the area of the member and that second-order effects resulting from load redistribution were a function of eccentricity created when half the member was severed. Thus, a smaller channel carried proportionally smaller loads and would be proportionally spaced, as well, causing similar behavior but on a smaller scale. This means that when the results were plotted as a ratio of the second-order moment (caused by the load redistribution) to the nominal moment, Pe, the results for the larger

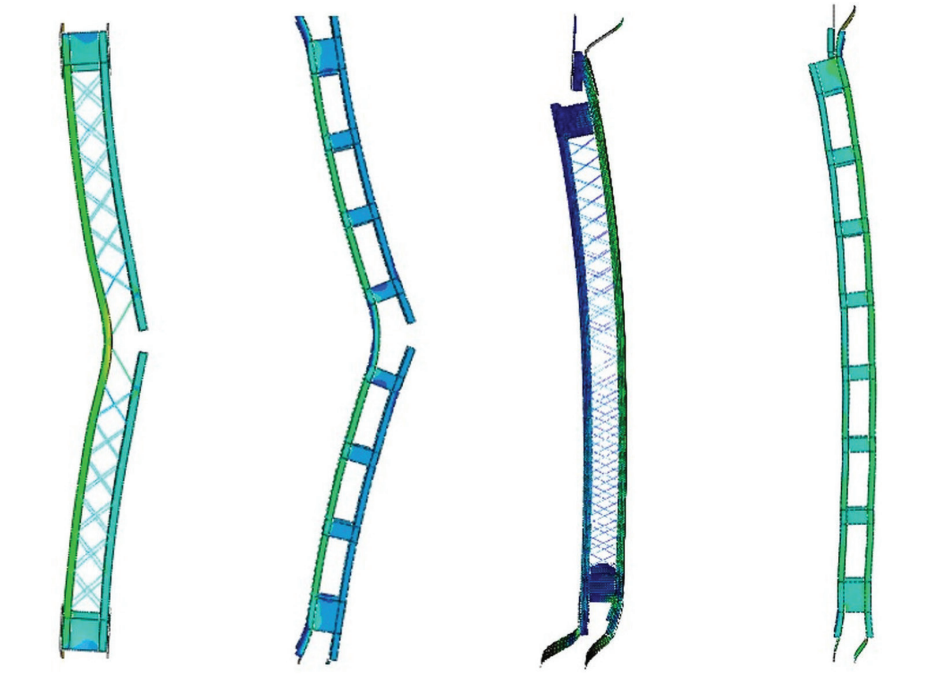

(a) Laced with mid-panel failure

(b) Stay-plated with mid-panel failure

(c) Laced with end failure near gusset

(d) Stay-plated with end failure near gusset

Fig. 21. Noncontinuous FEM results with deformations amplified 50 times for clarity.

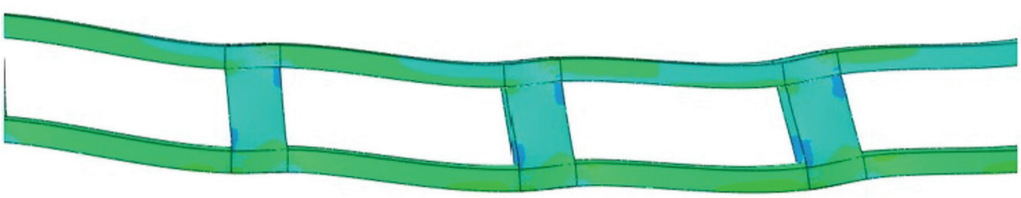

Fig. 22. Close-up of stay-plated member with deformations amplified 50 times, showing reverse curvature of the channels.

and smaller channel sections were nearly indistinguishable. This was the result for both continuous and noncontinuous members.

In addition to channel size, the spacing between channel pairs was studied. This parameter ranged from a spacing equal to half the depth of the channel up to two times the depth of the channel. When resulting second-order moments were normalized by the theoretical moment, *Pe*, then it appeared that as the spacing increased, the resulting moment decreased. However, when the second-order moments were not normalized, and instead absolute magnitudes were compared for geometries having different channel spacing, then it became clear that channel spacing had negligible effect on the results. The larger theoretical moment (i.e., *Pe*) was simply reducing the ratio of FEA moment to theoretical moment, due to the larger eccentricity, *e*.

This observation goes against the assumption that when one of the components fails the resulting second-order moment is equal to the original load times the faulted member eccentricity. The present parametric study found that such an assumption would be overly conservative for any two-channel geometry; as the spacing between components increased, that assumption would become increasingly overly conservative.

The panel length, which refers to the distance taken from centerline of a panel point to centerline of the next panel point for continuous members, or the length of the channels themselves for noncontinuous members, was found to have negligible effect on the after-fracture moment. Due to the localized curvature of the channels at the edges of stay plates that generated hotspots in the intact channel, longer spans having similar clear distances between stay plates were observed to have negligible effect. For laced members there were negligible increases in the resulting moments with longer member lengths. For example, doubling the panel length in some cases increased the after-fracture moment by 2%.

The thickness and length of the stay plates had negligible effect on the results. The thickness of the plates ranged from ⅜ to ⅞ in. The lengths of the plates ranged from half the depth of the channel to two times the depth of the channel. This range included a mixture of end and intermediate stay plates that would have exceeded known minimum design provisions. However, the results were insensitive to these changes in stay plate parameters. Existing design provisions also state that each plate must be fastened to the flanges of primary components with a minimum of three rivets per side. This type of connection would offer in-plane rotational constraint engaging the stay plates in resisting opening of the failed component as was observed during experimental testing.

In the FEMs, the connection was modeled using surface-to-surface tie constraints between shell elements, which constrained displacements and rotational degrees of freedom. Hence, modeled rotational constraint would be similar to that found on real structures, though most likely stiffer since slip at the highest loads on a riveted connection would not be allowed with the tie constraint such as was observed to occur on Specimen 1 in the laboratory test. The consequence of having stiffer stay plate connections is a larger localized transferal of moment into the intact channel. This means any difference in the FEM results caused by stiffer stay plate connections would have a conservative effect on the simplified solutions. However, it is important to keep in mind that laboratory testing showed that slip at the stay plates did not occur until near peak loads were reached, well beyond original design loads, and only for Specimen 1 when cut near the gusset connection. Specimen 2 showed no evidence of yielding and very minor evidence of slip at completion of testing in the stay plates adjacent to the failure location. The effectiveness of the stay plates in load redistribution is directly dependent upon the rotational constraint. This implies that stay plates have a minimum length to remain effective, but anything equal to or greater than half the depth of the channels to which they are attached with a minimum of three fasteners will effectively redistribute load. End stay plates were found to slightly reduce moments near the gusset connections for laced members but did not affect the secondary moment at the mid-panel location for mid-panel failures.

The number of stay plates within a given panel length was also studied and found to have a negligible effect. Smaller clear distances between stay plates resulting from increasing the number of stay plates, produced stiffer sections of channel between plates. Tripling the number of stay plate pairs was found to increase results by only 2–5%.

Lacing bar thickness, length, and spacing were investigated for their effect on laced two-channel members. Lattice bars sizes ranged from ⅛ to ¾ in. thick. Lattice fastener spacing ranged from half of the channel spacing to two times the channel spacing. Early design provisions limited the lattice spacing to about 45°, which would be equal to the channel spacing. The same provisions also called for a lattice thickness-to-length ratio of no more than 1/60. The parametric study varied this ratio from 1/169 to 1/28. It was found that these parameters all had negligible effects. One model was also analyzed in which the lattice bars were completely removed so that it only had the end stay plates. When the failure was at the mid-panel location of the member, the resulting moment at the location of the failure was reduced by about half compared to the same geometry with lattice bars, but the moment at the end stay plate was unaltered. When the failure was located between the end stay plate and the gusset connection of the member without lattice bars, the resulting moment at the mid-panel location was unchanged and the moment at the location of failure increased, going from 5% to about 9% of *Pe*. This behavior

suggests that while the lattice may support some limited load redistribution, it is not critical to performance of the member in the faulted condition. This also suggests that even though the parametric study focused on double lattice with fastened intersections, less robust systems of lattice, such as single lattice, would not be expected to affect results significantly. This comparison suggests that the simplified method of analysis resulting from the parametric study can be used for laced members of all kinds—that is, double or single lattice configurations.

The final parameter studied was the location of the failure. It included the mid-panel location and a location between the end stay plate and the gusset plate connections. Figure 23 shows four examples, one from each of the locations for each type of member. Figure 23(a) is failed between the end stay plate and gusset plate on a laced member. Figure 23(b) is failed between the end stay plate and gusset plate on a stay-plated member. Figure 23(c) shows the mid-panel failure for a laced member where the two lattice bars that would have connected into the location of the failure have been removed to facilitate convergence of the finite element solution. This was done for all laced member mid-panel failure models. Figure 23(d) shows a typical mid-panel failure for the stay-plated members. The resulting moment in laced members was not significantly affected by the location of the failure. This means that the resulting moment was always largest at the location of failure; however, the magnitude was not necessarily larger for mid-panel failures versus failures near the gusset plate. The same cannot be said for stay-plated types. It was found that failures near the gusset connection for both continuous and non-continuous stay-plated members resulted in moments that were two to three times larger than for the same geometry failed near mid-panel point. There were a few exceptions to this observation, so most models were analyzed two times, once with a failure at each location to ensure the worst-case scenario was captured for a given geometry. Plots of the percent of *Pe* in the following sections include results for both failure locations, which is the primary source of the data scatter.

Simplified Solution for Continuous Stay-Plated Two-Channel Members

Figure 24 compiles the results for all continuous, stay-plated models analyzed. The vertical axis is the finite element analysis moment divided by the theoretical moment, *Pe*. The horizontal axis is a combination of geometric properties used to correlate the results for the simplified solution. They offer simplistic inputs available to the engineer without refined analysis that can be readily taken from field

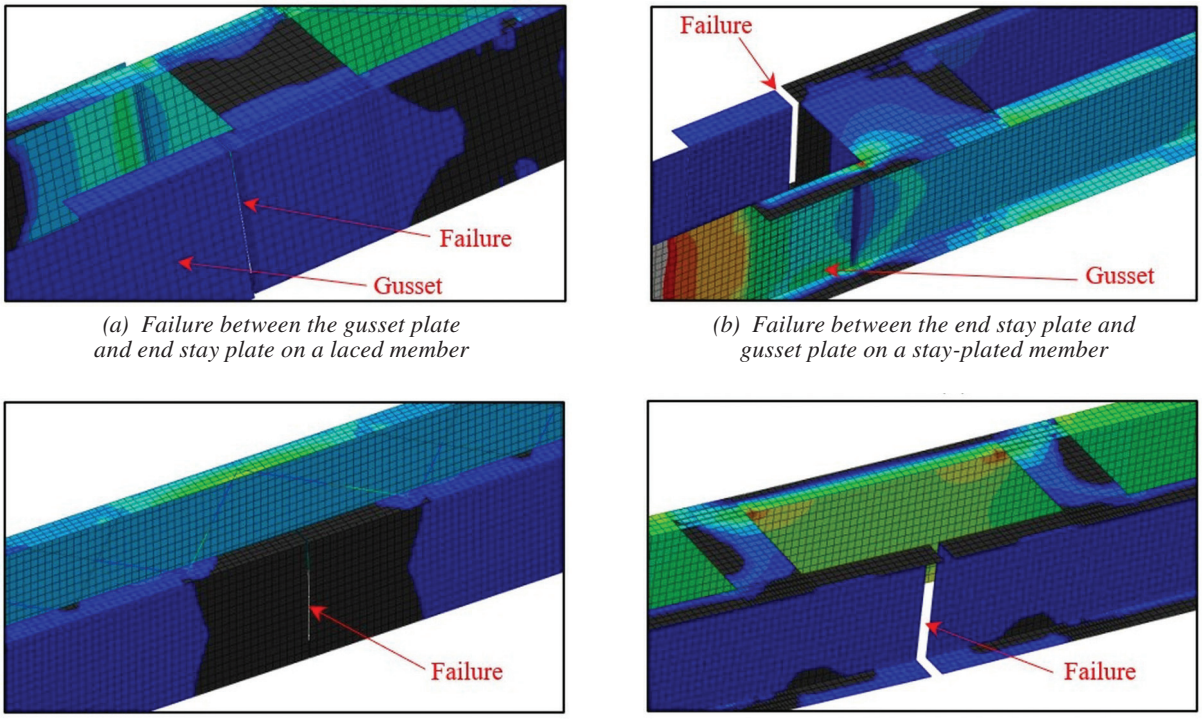

(a) Failure between the gusset plate and end stay plate on a laced member

(b) Failure between the end stay plate and gusset plate on a stay-plated member

(c) Mid-panel failure on a laced member

(d) Mid-panel failure on a stay-plated member

Fig. 23. Images depicting failure locations for stay-plated and laced two-channel members.

measurements or design drawings. The correlation includes the number of stay plate pairs (meaning a pair of plates located at the top and bottom of the member at the same cross section) within a single panel length, which includes the two end stay plate pairs and all intermediate stay plate pairs on the section of the member being evaluated, times the ratio of the channel depth to the channel spacing. The data plotted include all failure cases, both adjacent to the gusset plates and at the mid-section of the member. Failure cases closest to the gussets typically resulted in larger after-fracture moments, which is the primary cause for the scatter. The data show that an assumption of a secondary moment being generated equal to the axial load in the member times the eccentricity of the faulted member, or *Pe*, is overly conservative. As can be seen in Figure 24, most data were less than 10% of the *Pe* moment, with the most extreme case being less than 25%. Due to the regression analysis producing an equation fit to the maximum moments, the use of Equation 1 will provide a conservative estimate of the after-fracture moment.

Regression analysis was used to conservatively fit a line to the maximum values. The line is defined by Equation 1, which can be used to calculate the second-order moment resulting from a failed channel in a continuous, stay-plated, two-channel member.

$$M_{AF} = \frac{P_u e}{120}\left(\frac{N_{SP} d_{CH}}{2e} + 3\right) = \frac{P_u N_{SP} d_{CH} + 6P_u e}{240} \quad (1)$$

where

M_{AF} = after-fracture moment resulting from failure of a channel in a two-channel member (kip-in.)

P_u = total factored axial load (kips)

N_{SP} = number of stay plate pairs (1 pair equals the top and bottom stay plates at the same cross section) within the span of the member between the panel points

d_{CH} = depth of the channels (in.)

e = distance measured from the centroid of the unfaulted two-channel member to the centroid of the intact channel in the faulted state (in.); see Figure 17.

The resulting after-fracture moment is inserted into Equation 5 to calculate the after-fracture net section stress used to determine the remaining fatigue life. The individual results of each FEM can be viewed in the appendix reported by Lloyd et al. (2019).

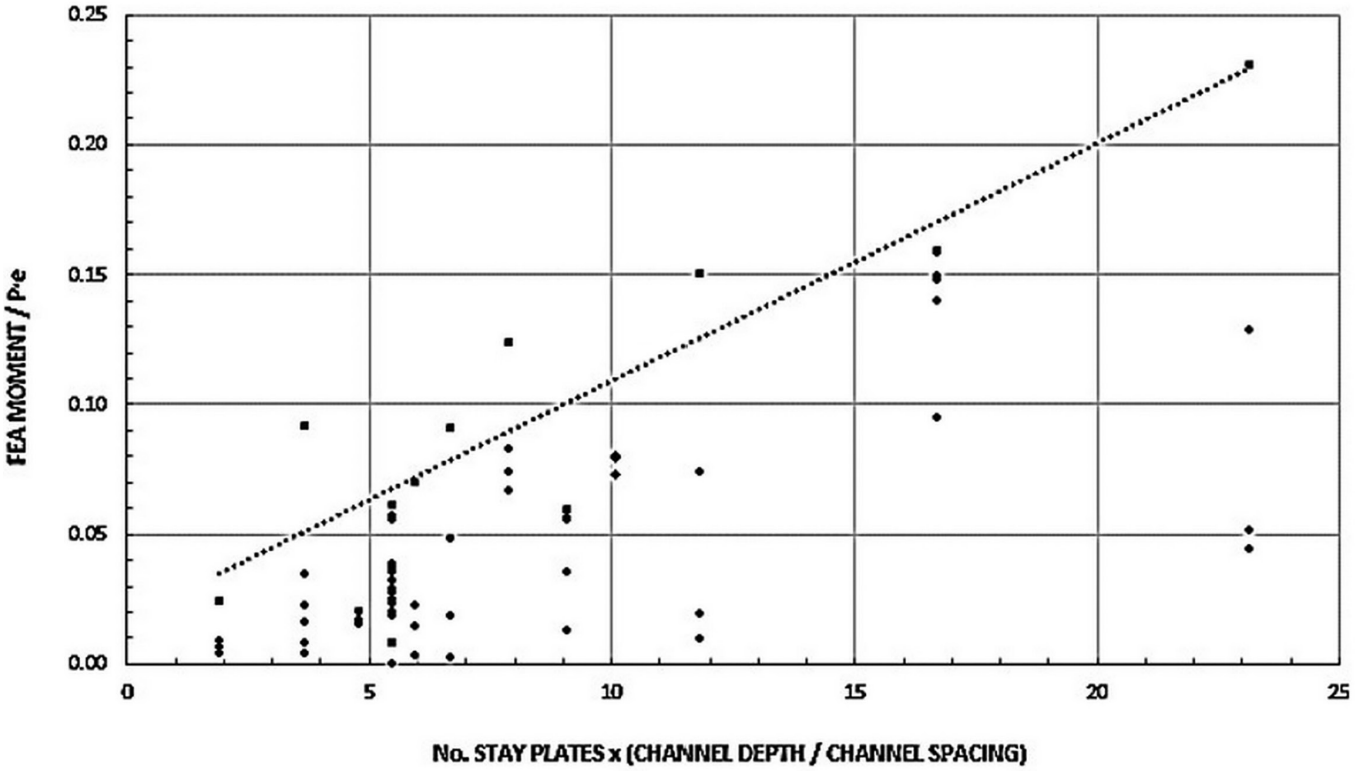

Fig. 24. Plot of results for continuous stay-plated two-channel members.

Simplified Solution for Continuous Laced Two-Channel Members

Figure 25 compiles the results for all continuous, laced models analyzed. The vertical axis is the finite element analysis moment divided by the theoretical moment, *Pe*. The horizontal axis is a combination of geometric properties used to correlate the results for the simplified solution. The parameters plotted offer simplistic inputs available to the engineer without refined analysis that can be readily obtained from field measurements or design drawings. These correlation parameters include the length in inches from the centerline of a panel point to the centerline of the next panel point divided by the lattice spacing, times the ratio of the channel depth to the channel spacing.

Regression analysis was used to conservatively fit a line to the maximum values. The line is defined by Equation 2, which can be used to calculate the second-order moment resulting from a failed channel in a continuous, laced, two-channel member. The lattice bar configuration factor, γ_{LB}, accounts for the difference between single lattice bar and double lattice bars spacing. Equation 2 was derived using double lattice bar spacing. Based on results for members where the lattice was removed, the simplified method can be extended to single lattice configurations, as well. Thus, the lattice bar configuration factor reduces the spacing of single lattice bar members to an equivalent double lattice bar spacing such that the moment is not incorrectly doubled for single lattice members. Finally, as can be seen in Figure 25, the maximum moment reaches a plateau of less than 14% of *Pe* for all modeled geometries, including the most extreme geometric cases studied (i.e., longest and narrowest member configurations). Therefore, Equation 2 puts a practical limit on the moment of 0.15*Pe*. The data plotted include all failure cases (i.e., adjacent to the gusset plates and at the mid-section of the member). Unlike for stay-plated members, laced member failure cases closest to the gussets were not necessarily observed to produce larger after-fracture moments. Hence, the data scatter is reduced for laced member types. The data further illustrate that an assumption of a secondary moment being generated equal to the axial load in the member times the eccentricity of the faulted member, or *Pe*, is overly conservative. As can be seen in Figure 25, most data were less than 10% of the *Pe* moment, with the most extreme cases staying below 14%.

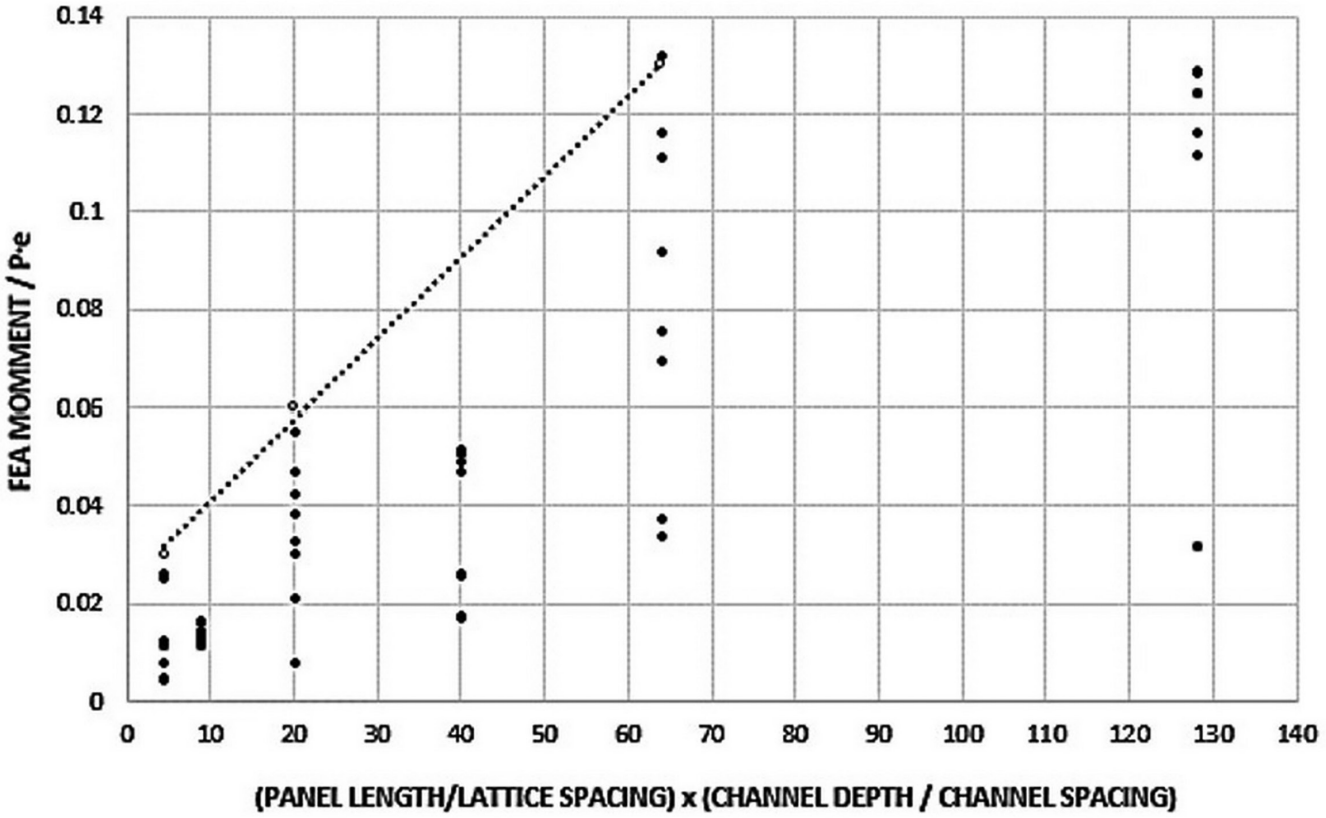

Fig. 25. Plot of results for continuous laced two-channel members.

Due to the regression analysis producing an equation fit to the maximum moments, the use of Equation 2 will provide a conservative estimate of the after-fracture moment.

$$M_{AF} = \frac{P_u e}{590}\left(\frac{L_{PL} d_{CH}}{\gamma_{LB} S_{LB} 2e} + 14\right) \tag{2}$$

$$= \frac{P_u L_{PL} d_{CH} + 28 P_u e \gamma_{LB} S_{LB}}{1{,}180 \gamma_{LB} S_{LB}} \leq 0.15 P_u e$$

where

L_{PL} = length of the panel measured between the centerlines of two panel points (in.)

M_{AF} = after-fracture moment resulting from failure of a channel in a two-channel member (kip-in.)

P_u = total factored axial load (kips)

S_{LB} = spacing of the lattice bars measured longitudinally between centerlines of fasteners connecting the lattice bars to a channel flange (in.)

d_{CH} = depth of the channels (in.)

e = distance measured from the centroid of the unfaulted two-channel member to the centroid of the intact channel in the faulted state (in.); see Figure 17.

γ_{LB} = lattice bar configuration factor; 1.0 for double lattice, 0.5 for single lattice

The resulting moment is inserted into Equation 5 to calculate the after-fracture net section stress used to determine the remaining fatigue life. The individual results of each FEM can be viewed in the appendix reported by Lloyd et al. (2019).

Simplified Solution for Noncontinuous Stay-Plated Two-Channel Members

Figure 26 compiles the results for all noncontinuous, stay-plated models analyzed. The vertical axis is the finite element analysis moment divided by the theoretical moment, *Pe*. Once again, the horizontal axis is a combination of geometric properties used to correlate the results for the simplified solution. Again, these parameters are based on input data that are readily available to the engineer without refined analysis that can be easily obtained from field measurements or design drawings. It is the number of stay plate pairs (meaning a pair of plates located at the top and bottom of the member at the same cross section) along the entire length of the member, which includes each of the two end stay plate pairs and all intermediate stay plate pairs on the section of the member being evaluated, times the ratio of the channel depth to the channel spacing.

Regression analysis was used to conservatively fit a line to the maximum values. The line is defined by Equation 3, which can be used to calculate the second-order moment resulting from a failed channel in a noncontinuous, stay-plated, two-channel member. The moment is limited to 0.35*Pe*, which is slightly above the maximum value observed for the continuous laced member geometries

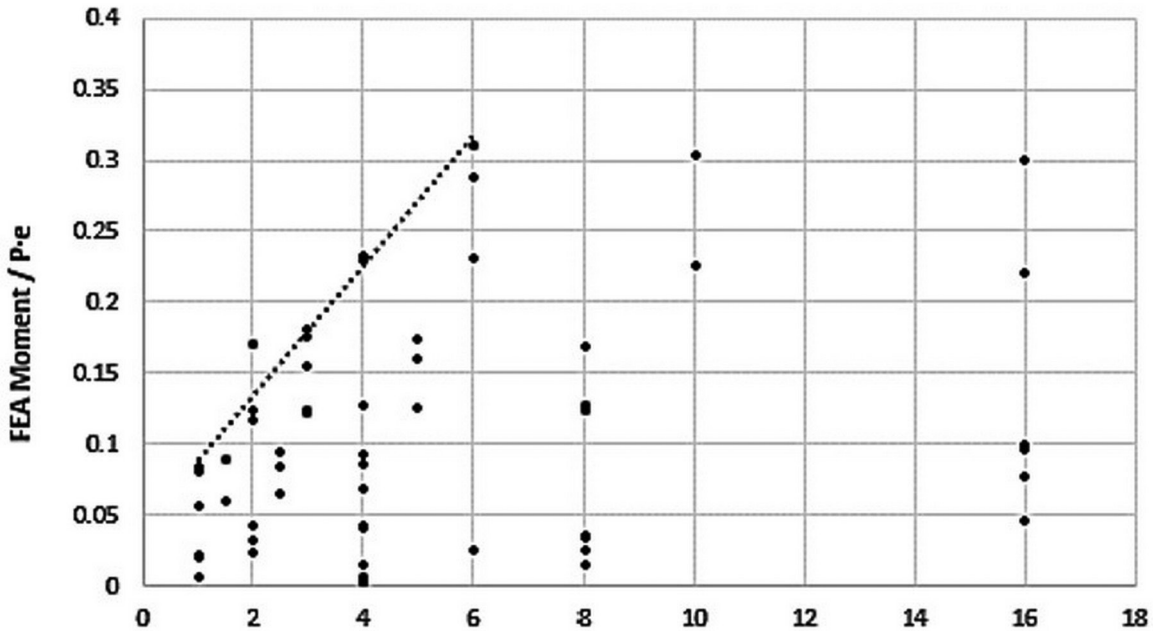

Fig. 26. Plot of results for noncontinuous stay-plated two-channel members.

studied, as can be seen in Figure 26. The maximum after-fracture moments for the noncontinuous stay-plated members were generally larger than those for the continuous stay-plated members by approximately 15–20%. The continuous stay-plated members benefited from the continuity across nodes through which they could distribute moment, whereas the noncontinuous types were forced to carry the entire after-fracture moment within the intact channel at the location of failure without benefit of continuity.

$$M_{AF} = \frac{P_u e}{22}\left(\frac{N_{SP} d_{CH}}{2e} + 1\right) \tag{3}$$
$$= \frac{P_u N_{SP} d_{CH} + 2P_u e}{44} \le 0.35 P_u e$$

where

M_{AF} = after-fracture moment resulting from failure of a channel in a two-channel member (kip-in.)

N_{SP} = number of stay plate pairs (1 pair equals the top and bottom stay plates at the same cross section) within the span of the member between the panel points

P_u = total factored axial load (kips)

d_{CH} = depth of the channels (in.)

e = distance measured from the centroid of the unfaulted two-channel member to the centroid of the intact channel in the faulted state (in.); see Figure 17.

The resulting moment is inserted into Equation 5 to calculate the after-fracture net section stress used to determine the remaining fatigue life. The individual results of each FEM can be viewed in the appendix reported by Lloyd et al. (2019).

Simplified Solution for Noncontinuous Laced Two-Channel Members

Figure 27 compiles the results for all noncontinuous laced models analyzed. The vertical axis is the finite element analysis moment divided by the theoretical moment, *Pe*. The horizontal axis is a combination of geometric properties used to correlate the results for the simplified solution. They offer simple inputs that don't require advanced analysis tools. It is the length (in.) of the channels, including the depth into the gusset plate at each end of the member, divided by the lattice bar spacing, times the ratio of the channel depth to the channel spacing.

Regression analysis was used to conservatively fit a line to the maximum values. The data plotted include all failure

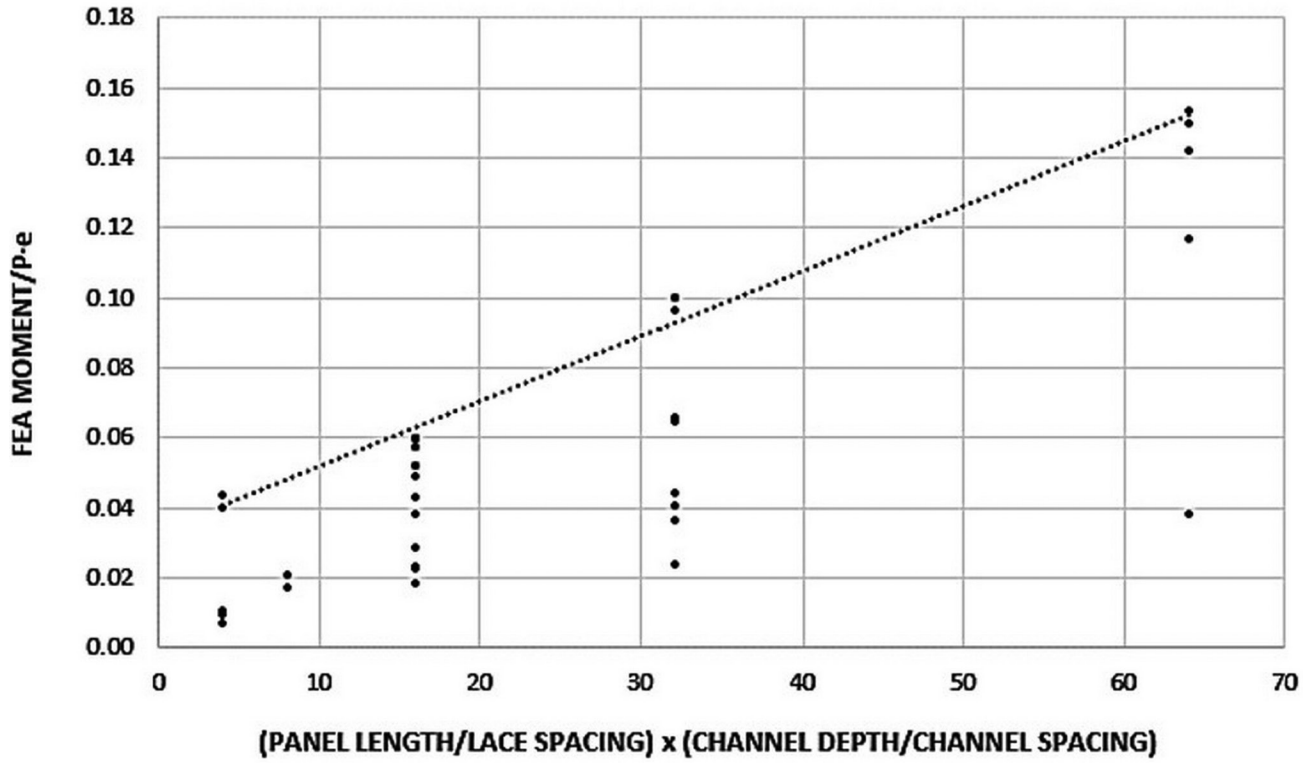

Fig. 27. Plot of results for noncontinuous laced two-channel members.

cases (i.e., adjacent to the gusset plates and at the mid-section of the member). Unlike for stay-plated members, laced member failure cases closest to the gussets were not necessarily observed to produce larger after-fracture moments. Hence, once again the data scatter is reduced for the noncontinuous laced member type. The data in Figure 27 further illustrate that an assumption of a secondary moment being generated equal to the axial load in the member times the eccentricity of the faulted member, or *Pe*, is overly conservative. As can be seen, most data were below 10% of a theoretical *Pe* moment, with the most extreme cases staying below 14%. Due to the regression analysis producing an equation fit to the maximum moments, the use of Equation 4 will provide a conservative estimate of the after-fracture moment. The line in Figure 27 is defined by Equation 4, which can be used to calculate the second-order moment resulting from a failed channel in a noncontinuous, laced, two-channel member. The lattice bar configuration factor, γ_{LB}, accounts for the difference between single lattice bar and double lattice bars spacing. Equation 4 was derived using double lattice bar spacing. Based on results for members where the lattice was removed, the simplified method can be extended to single lattice configurations, as well. Thus, the lattice bar configuration factor reduces the spacing of single lattice bar members to an equivalent double lattice bar spacing such that the moment is not incorrectly doubled for single lattice members.

$$M_{AF} = \frac{P_u e}{550}\left(\frac{L_{PL} d_{CH}}{\gamma_{LB} S_{LB} 2e} + 20\right) = \frac{P_u L_{PL} d_{CH} + 40 P_u e \gamma_{LB} S_{LB}}{1{,}100 \gamma_{LB} S_{LB}} \quad (4)$$

where

L_{PL} = length of the panel measured between the centerlines of two panel points (in.)

M_{AF} = after-fracture moment resulting from failure of a channel in a two-channel member (kip-in.)

P_u = total factored axial load (kips)

S_{LB} = spacing of the lattice bars measured longitudinally between centerlines of fasteners connecting the lattice bars to a channel flange (in.)

d_{CH} = depth of the channels (in.)

e = distance measured from the centroid of the unfaulted two-channel member to the centroid of the intact channel in the faulted state (in.); see Figure 17.

γ_{LB} = lattice bar configuration factor; 1.0 for double lattice, 0.5 for single lattice

The resulting moment is inserted into Equation 5 to calculate the after-fracture net section stress used to determine the remaining fatigue life. The individual results of each FEM can be viewed in the appendix reported by Lloyd et al. (2019).

Application of Parametric Study Findings for Two-Channel Members

The following describes implementation of the after-fracture moments, previously explained, to calculate the after-fracture net section stress resulting from failure of a channel in a two-channel member.

After-Fracture Net Section Stress Calculation

Following calculation of the after-fracture moment that results from failure of one of the two channels, Equation 5 is used to calculate the after-fracture net section stress. The equation combines the axial net section stress and second order flexural stress. The axial net section stress is the total factored load carried by the member in the unfaulted state, divided by the after-fracture net section. The flexural stress is the after-fracture moment calculated using one of Equations 1 to 4, as applicable for the member type, times the distance from the neutral axis to the point of interest, c, divided by the weak-axis moment of inertia, I_y, of the intact channel.

$$f_{AFN} = \frac{P_u}{A_{AFN}} + \frac{M_{AF} c}{I_y} \quad (5)$$

where

A_{AFN} = net section area of the member in the faulted state; this is equal to the net area of a single channel (in.^{2})

I_y = principal axis moment of inertia about the weak axis of a single channel (in.^{4})

M_{AF} = after-fracture moment resulting from failure of a channel in a two-channel member (kip-in.)

P_u = total factored applied tensile load (kips)

c = distance from the centroid of the channel to the surface of stress calculation (in.)

f_{AFN} = factored total net section stress in the faulted state (ksi)

Guidance for Use of Simplified Solutions for Two-Channel Members

The simplified method of analysis was developed considering failures at mid-panel and near the gusset connections capturing the largest resulting moments for the geometries analyzed. This means that a single after-fracture moment calculation and net section stress calculation need to be performed for each member. There is no need to repeat this calculation multiple times for different cross sections of the same member. Figures 28 and 29 illustrate two generic types of trusses where two-channel members could be used. Figure 28 shows a three-span continuous deck truss structure. Figure 29 depicts a single-span through-truss structure. Each figure has been highlighted with red and blue lines. The red lines indicate members that would be analyzed

using either Equation 1 (stay-plated) or 2 (laced) for continuous members. The blue lines designate members that would be evaluated using either Equation 3 (stay-plated) or 4 (laced) for noncontinuous members. Members that are *not* highlighted, or which appear black, are compression members that would not need to be evaluated for internal redundancy. Reversal zones that are subjected to both tensile and compressive live load stresses would also need to be evaluated. Notice that the terminating bottom chord of each truss is evaluated using equations for noncontinuous members. Due to the lack of continuity beyond the abutment at each end of a truss, the last panel should be analyzed using equations developed for noncontinuous members.

CONCLUSIONS

This paper summarizes the experimental and analytical research into behavior of mechanically fastened built-up axial steel members comprised of two rolled channels following fracture of a single channel. Previously performed and reported-on fracture tests verified cross-boundary fracture resistance (CBFR) of axially loaded built-up steel members as evidence that these member types can avoid full cross-section fracture in service (Lloyd et al., 2021). Finite element–based parametric studies were conducted to characterize the static load redistribution behavior of two-channel axial members following a fracture event. Finite element models (FEMs) were calibrated using experimental data obtained from full-scale testing. Simplified solutions were developed to estimate the after-fracture load capacity and the fatigue stress range in the remaining channel, accounting for second-order moments. The solutions can be applied to internal redundancy evaluations. If a member is found to be internally redundant, the solutions can then be used to reliably predict fatigue life of the member in the faulted state and establish the special inspection interval according to the provisions of AASHTO (2018).

The research concluded that mechanically fastened built-up axial members comprised of two rolled channels can possess sufficient strength and fatigue resistance after the failure of a single channel. After-fracture load redistribution behavior of two-channel members was found to result in a global out-of-plane flexural response in the surviving channel. Applied boundary conditions were significantly influential on some member types, driving separate simplified solutions for continuous and noncontinuous two-channel members. The derived solutions calculate the after-fracture, second-order moment carried by the surviving channel in combination with the original and redistributed axial loads. A verification exercise comparing results from the derived solutions back to full-scale experimental research predicted primary longitudinal stress to within a few percentage points of the measured values at locations of interest. As a result, it was concluded that the proposed method of analysis contained herein provides a simple, conservative, and efficient quantitative approach to perform the redundancy analysis and the prediction of the commensurate special inspection interval.

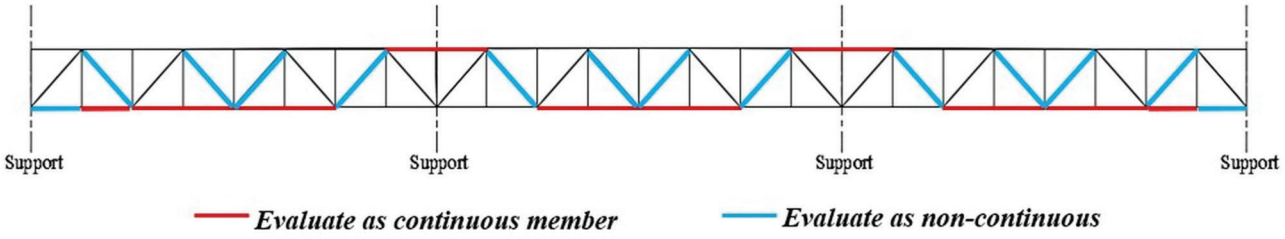

Fig. 28. Sketch illustrating correct application of Equations 1–4 on continuous trusses.

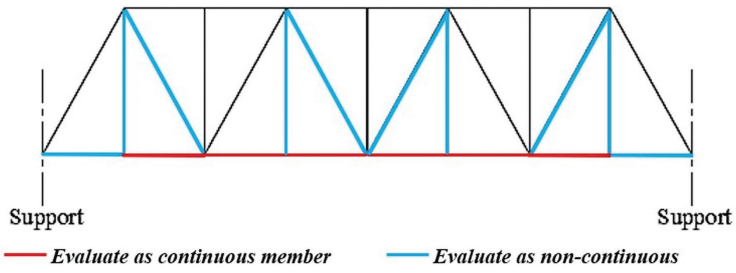

Fig. 29. Sketch illustrating correct application of Equations 1–4 on simple span trusses.

REFERENCES

AASHO (1935), *AASHO Standard Specifications for Highway Bridges*, 2nd ed., The American Association of State Highway Officials, Washington D.C.

AASHTO (2018), *AASHTO Guide Specifications for Internal Redundancy of Mechanically-Fastened Built-Up Steel Members*, 1st ed., American Association of State Highway and Transportation Officials, Washington D.C.

AASHTO (2020), *LRFD Bridge Design Specifications*, 9th ed., American Association of State Highway and Transportation Officials, Washington, D.C.

AREMA (2017), *AREMA Manual for Railway Engineering*, American Railway Engineering and Maintenance-of-Way Association, Lanham, Maryland

ASTM (2016a), *Standard Test Methods for Notched Bar Impact Testing of Metallic Materials*, ASTM E23, ASTM International, West Conshohocken, Pa.

ASTM (2016b), *Standard Test Methods for Tension Testing of Metallic Materials*, ASTM E8, ASTM International, West Conshohocken, Pa.

ASTM (2017), *Standard Test Method for Analysis of Carbon and Low-Alloy Steel by Spark Atomic Emission Spectrometry*, ASTM E415, ASTM International, West Conshohocken, Pa.

ASTM (2019), *Standard Specification for High Strength Structural Bolts and Assemblies, Steel and Alloy Steel, Heat Treated, Inch Dimensions 120 ksi and 150 ksi Minimum Tensile Strength, and Metric Dimensions 830 MPa and 1040 MPa Minimum Tensile Strength*, ASTM F3125/F3125M-19e2, ASTM International, West Conshohocken, Pa.

Campbell, L.E., Snyder, L.R., Whitehead, J.M., Connor, R.J., and Lloyd, J.B. (2019), "Probability of Detection Study for Visual Inspection of Steel Bridges: Volume 2—Full Project Report," Joint Transportation Research Program Publication No. FHWA/IN/JTRP-2019/22, Purdue University, West Lafayette, Ind. https://doi.org/10.5703/1288284317104

Connor, R.J., Dexter, R., and Mahmoud, H. (2005), *NCHRP Synthesis 354: Inspection and Management of Bridges with Fracture-Critical Details,* Washington D.C., p. 84.

Diggelmann, L.M., Connor, R.J., and Sherman, R.J. (2013), *Evaluation of Member and Load-Path Redundancy on the US-421 Bridge over the Ohio River*, Washington D.C.

FHA (1988), "National Bridge Inspection Standards," *Federal Register*, Vol. 53, No. 121, p. 23,611.

FHA (2022), "National Bridge Inspection Standards," *Federal Register*, Vol. 87, No. 88, p. 27,396.

Hebdon, M.H., Bonachera Martin, F.J., Korkmaz, C., and Connor, R.J. (2017), "Fracture Resilience of Steel Built-Up Members Subjected to Flexure," *Journal of Bridge Engineering*, ASCE. DOI: 10.1061/(ASCE)BE.1943-5592.0001059

Lloyd, J.B., Bonachera Martin, F.J., Korkmaz, C., and R.J. Connor (2021), "Internal Redundancy of Mechanically-Fastened Built-Up Steel Axially-Loaded Multi-Component Members," *Journal of Bridge Engineering*, ASCE. DOI: 10.1061/(ASCE)BE.1943-5592.0001743

Lloyd, J.B., Campbell, L.E., Bonachera Martin, F.J., and Connor, R.J. (2019), "Experimental and Analytical Evaluation of the Strength of Selected Truss Members from the Approach Spans of the Winona Bridge," Purdue University, West Lafayette, Ind. https://doi.org/10.5703/1288284316925

Mekker, M.M., Remias, S.M., McNamara, M.L., and Bullock, D.M. (2015), *Characterizing Interstate Crash Rates Based on Traffic Congestion Using Probe Vehicle Data*, Transportation Research Board, Washington, D.C. http://docs.trb.org/prp/16-1194.pdf

Ocel, J.M. (2013), NCHRP Web-Only Document 197: *Guidelines for the Load and Resistance Factor Design and Rating of Riveted and Bolted Gusset-Plate Connections for Steel Bridges*, Transportation Research Board, Washington D.C.